

NASA TECHNICAL NOTE



N71-20195
NASA TN D-6114

NASA TN D-6114

CASE FILE
COPY

A STUDY OF THE MIXING OF
HYDROGEN INJECTED NORMAL
TO A SUPERSONIC AIRSTREAM

by R. Clayton Rogers
Langley Research Center
Hampton, Va. 23365



1. Report No. NASA TN D-6114	2. Government Accession No.	3. Recipient's Catalog No.	
4. Title and Subtitle A STUDY OF THE MIXING OF HYDROGEN INJECTED NORMAL TO A SUPERSONIC AIRSTREAM		5. Report Date March 1971	6. Performing Organization Code
		8. Performing Organization Report No. L-7386	
7. Author(s) R. Clayton Rogers		10. Work Unit No. 722-03-10-01	11. Contract or Grant No.
9. Performing Organization Name and Address NASA Langley Research Center Hampton, Va. 23365		13. Type of Report and Period Covered Technical Note	
		14. Sponsoring Agency Code	
12. Sponsoring Agency Name and Address National Aeronautics and Space Administration Washington, D.C. 20546		15. Supplementary Notes The information presented herein was included in a thesis entitled "The Penetration and Mixing of a Sonic Hydrogen Jet Injected Normal to a Mach 4 Airstream" offered in partial fulfillment of the requirement for the degree of Master of Science in Aerospace Engineering, Virginia Polytechnic Institute, Blacksburg, Virginia, March 1970.	
16. Abstract <p>An investigation has been conducted to determine the effect of the ratio of jet dynamic pressure to free-stream dynamic pressure, in the range of 0.5 to 1.5, on the penetration and mixing of a sonic hydrogen jet injected normal to a Mach 4 airstream. Free-stream conditions consisted of a stagnation temperature of 300 K and stagnation pressures of 13.6 and 20.4 atmospheres (1 atmosphere = 101.325 kN/m²). Turbulent boundary-layer thickness at the injection station was 2.70 injector diameters. Measurements of hydrogen volume fraction and pitot pressure were made at downstream stations between 7 and 200 injector diameters. As a result of the investigation, it was found that the penetration trajectory was proportional to the 0.3 power of the dynamic-pressure ratio and the decay of the maximum concentration (to values of 0.1) was inversely proportional to the square root of the downstream distance. Nondimensional concentration profiles for the vertical surveys were approximated by Gaussian-type functions and showed similarity at stations equal to or greater than 60 injector diameters.</p>			
17. Key Words (Suggested by Author(s)) Injection Jet mixing Supersonic combustion		18. Distribution Statement Unclassified - Unlimited	
19. Security Classif. (of this report) Unclassified	20. Security Classif. (of this page) Unclassified	21. No. of Pages 53	22. Price* \$3.00

A STUDY OF THE MIXING OF HYDROGEN INJECTED NORMAL TO A SUPERSONIC AIRSTREAM*

By R. Clayton Rogers
Langley Research Center

SUMMARY

An investigation has been conducted on the penetration and mixing of hydrogen injected normal to a supersonic airstream with the ratio of jet dynamic pressure to free-stream dynamic pressure varied from 0.5 to 1.5. Hydrogen gas was injected at sonic velocity from a circular injector in a flat plate into a Mach 4.03 airstream at a stagnation temperature of 300 K and stagnation pressures of 13.6 and 20.4 atmospheres (1 atmosphere = 101.325 kN/m²). Corresponding Reynolds numbers per meter were 6.19×10^7 and 9.28×10^7 , respectively, and resulted in a turbulent boundary-layer thickness of 2.70 injector diameters at the injector station. Measurements of hydrogen volume fraction and pitot and static pressures were made at downstream stations of 7, 30, 60, 120, and 200 injector diameters and yielded mass fraction, Mach number, stagnation pressure, velocity, and mass flux profiles. Data correlations from the literature underpredicted the measured jet penetration; this underprediction is thought to be due, in part, to the relatively thick boundary layer of this investigation. At all downstream stations the penetration was found to be proportional to the 0.3 power of the dynamic-pressure ratio and the decay of the maximum mass concentration (to values of 0.1) was inversely proportional to the square root of the downstream distance. At any particular station the maximum mass concentration was proportional to the 0.54 power of the dynamic-pressure ratio. Nondimensional concentration profiles for the vertical surveys were approximated by Gaussian-type functions and showed similarity at stations equal to or greater than 60 injector diameters.

INTRODUCTION

Advanced hypersonic vehicles, such as a reusable launch vehicle with an airbreathing propulsion system for the first stage, are currently under investigation. (See ref. 1.) The

*The information presented herein was included in a thesis entitled "The Penetration and Mixing of a Sonic Hydrogen Jet Injected Normal to a Mach 4 Airstream" offered in partial fulfillment of the requirement for the degree of Master of Science in Aerospace Engineering, Virginia Polytechnic Institute, Blacksburg, Virginia, March 1970.

proposed propulsion system is a hydrogen-fueled supersonic combustion ramjet with operation to a free-stream Mach number of 12, and a corresponding combustor entrance Mach number of approximately 4. The accurate analysis and design of the combustor requires a knowledge of the fuel-air mixing characteristics and a means of injecting the fuel so that a nearly uniform fuel distribution and a short mixing length are obtained without producing significant thrust penalties. These requirements suggest that parallel injection from multiple points in the stream (refs. 2 and 3) and normal injection from several points on the walls (ref. 4) will both be included in the optimized design.

Normal sonic injection of various gases and gaseous mixtures issuing from a discrete circular hole in the flat plate into a supersonic airstream has been investigated and reported in references 4 to 10. These data are generally for conditions corresponding to values of the ratio of jet dynamic pressure to free-stream dynamic pressure greater than 1.3 and indicate that for sonic injection, shorter mixing lengths occur at lower values of the ratio of jet dynamic pressure to free-stream dynamic pressure. Analytical methods presented in references 8 to 10 for predicting the penetration of the jet and the jet trajectory in the unconfined supersonic mainstream have been developed from empirical and semiempirical data correlations. Generally, these correlations do not consider any effect of the mainstream boundary-layer thickness.

The present investigation was conducted to provide detailed information on the penetration and mixing of hydrogen injected normal to a supersonic airstream with a thick boundary layer for values of the ratio of jet dynamic pressure to free-stream dynamic pressure from 0.5 to 1.5. These data are needed to aid in constructing analytical methods that yield reliable predictions of the mixing process in supersonic combustors.

The hydrogen gas was injected from a 0.102-centimeter-diameter sonic nozzle perpendicular to the surface of a flat plate mounted in a 23-centimeter-square tunnel test section. The tests were conducted at a free-stream Mach number of 4.03, stagnation temperature of 300 K, and stagnation pressures of 13.6 and 20.4 atmospheres and resulted in Reynolds numbers per meter of 6.19×10^7 and 9.28×10^7 , respectively (1 atmosphere = 101.325 kN/m²). Boundary-layer thickness on the flat plate at the injector station was 2.7 injector diameters. Ratios of jet dynamic pressure to free-stream dynamic pressure of 0.5, 0.75, 1.0, and 1.5 were investigated. Measurements of hydrogen volume fraction, pitot pressure, and static pressure were obtained by vertical and horizontal surveys of the flow field at downstream stations of 7, 30, 60, 120, and 200 injector diameters. The present data are compared with the previously obtained data correlations.

SYMBOLS

A streamtube cross-sectional area, meters²

b₁ exponent defined in equation (7)

2

b_2	exponent defined in equation (8)
C_D	drag coefficient
d	injector nozzle exit diameter, meters
d_j	equivalent jet exit diameter, $dK^{1/2}$, meters
f	fuel-air mass ratio
h	distance measured along center line of emerging jet, meters
K	injector nozzle discharge coefficient
M	Mach number
\dot{m}	mass flow rate, kilograms/second
N_{Re}	Reynolds number
p	absolute pressure, newtons/meter ² or atmospheres
q_r	ratio of jet dynamic pressure to free-stream dynamic pressure, $(\rho V^2)_j / (\rho V^2)_\infty$
T	absolute temperature, kelvin
V	velocity, meters/second
x	longitudinal coordinate
x_0	potential core length, meters
y	lateral coordinate
z	vertical coordinate
α	hydrogen mass fraction
β	air mass flux parameter, $(\rho V)_x(1 - \alpha)$, $\frac{\text{kilograms}}{\text{meter}^2\text{-second}}$
δ	boundary-layer thickness, meters
δ^*	boundary-layer displacement thickness, meters
θ	slope of emerging jet center line measured from horizontal, degrees

θ_i	initial slope of injector, degrees
λ	ratio of jet mass flux to free-stream mass flux, $(\rho V)_j / (\rho V)_\infty$
ν	hydrogen volume fraction
ξ	hydrogen mass flow rate parameter, $\alpha(\rho V)_x / (\rho V)_j$
ρ	mass density, kilograms/meter ³

Subscripts:

∞	free-stream conditions
o	conditions at edge of mixing region where $\nu = 0.005$
1	conditions in undisturbed flow upstream of injector
5	conditions at which the mass concentration is half maximum
j	jet conditions
t	stagnation conditions
x	survey point
max	maximum value
ref	reference value
α	conditions at which concentration is maximum

A bar over a symbol denotes an average quantity.

MODEL AND FACILITY

Test Apparatus and Model

A sketch of the stainless-steel rectangular flat plate used in the experiments is shown in figure 1. A 0.102-centimeter-diameter sonic nozzle was flush-mounted perpendicular to the plate surface 18.6 centimeters from the plate leading edge. Details of the nozzle are shown in figure 1. The plate leading edge was a 2° wedge tapering to a cylindrical leading edge of approximately 0.013-centimeter thickness, followed by a 10° wedge. The plate spanned the 23-centimeter by 23-centimeter test section of a continuous-flow supersonic tunnel. Additional information on the tunnel may be found in reference 4.

Boundary-layer profiles at the injector station with stagnation temperatures of 300 K and stagnation pressures of 13.6 and 20.4 atmospheres (unit Reynolds numbers of 6.19×10^7 and 9.28×10^7 per meter) are presented in figure 2. Also shown are theoretical results, computed from the method of reference 11 for the 20.4 atmosphere condition, which agree well with the data. The boundary-layer thickness based on an edge velocity of 99 percent of the free-stream value was 2.70 injector exit diameters for both free-stream stagnation pressures.

Injector Flow

A schematic of the hydrogen gas supply and control system is presented in figure 3. The system was equipped with pressure-controlled valves and purged with nitrogen. Total temperature of the jet was measured by using a standard iron-constantan thermocouple inserted in a filter between the orifice meter and the injector. Jet total pressure was measured near the injector by means of a wall static-pressure orifice mounted in the 0.476-centimeter-diameter injector supply tube. Calculations indicated that the measured pressure would be within 99 percent of the jet total pressure. A tube attached to the injector supply line supplied 100-percent hydrogen samples for full-scale chromatograph readings. During a survey, gas samples of the hydrogen-air mixture were taken through the pitot probe with the aid of a vacuum pump at mass flow rates up to 4.17 mg/sec. The sample flow to the chromatograph was metered to 0.0556 mg/sec and the remaining flow bypassed and discharged to the atmosphere. The apparatus was operated over a jet total-pressure range of 2 to 4 atmospheres corresponding to ratios of jet dynamic pressure to free-stream dynamic pressure of 0.5 to 1.5. Test conditions are presented in the following table:

Test condition	q_r	$p_{t,\infty}$, atm	$p_{t,j}$, atm	\dot{m}_j , g/sec	$N_{Re,\infty}$, m^{-1}	δ/d
1	0.50	20.4	1.986	0.0820	9.28×10^7	2.70
2	.75	20.4	2.980	.1230	9.28	2.70
3	1.00	13.6	2.647	.1094	6.19	2.70
4	1.50	13.6	3.960	.1641	6.19	2.70

Instrumentation

Gas analyzer. - The volumetric concentration of hydrogen in the gas samples was measured by a process gas chromatograph. (See refs. 12 and 13.) At the beginning of a 1-minute cycle, part of the sample gas was isolated and forced by the carrier gas, nitrogen, through a molecular sieve and a column consisting of a length of stainless-steel

tubing packed with silica gel. This procedure provided a qualitative identification of each component since each will process through the column at a predictable rate. The quantity of each component was determined by four thermal conductivity detectors of which two are always exposed to the carrier gas. The unbalance of the detector bridge provided a voltage output proportional to the cooling effect and hence was a measure of the concentration of the separated sample components relative to the carrier gas. The voltage output was recorded by a pen deflection on a strip chart. Readout controls were adjusted so that only the hydrogen concentration was detected.

Probe description.- The gas-sampling pitot probe and the static probe are shown in figure 4. The pitot-sampling probe is a boundary-layer survey type with the probe tip mounted in a 7.94-millimeter-diameter supporting tube offset to allow for actuator rod clearance. The actuator mechanism provided for probe movement for vertical traversing and yaw in the horizontal plane. The static-pressure probe was of similar design with a cone angle of 28° and four 0.203-millimeter orifices located at 14 probe diameters from the tip.

Flow measurement.- The mass flow of the injected gas was measured with a 0.318-centimeter-diameter, sharp-edged, corner-tap orifice meter. The static temperature at the meter was assumed to be the same as the jet stagnation temperature. Hydrogen mass flow rate through the orifice meter was calculated from an equation derived from a hydrogen-corrected air calibration of the orifice meter. The discharge coefficient of the injector nozzle, based on orifice meter measurements, normally ranged from 0.73 to 0.78 with an average value of 0.76. The sample flow rate to the chromatograph and the bypass flow rate were measured by thermoconductivity mass flow rate meters. All pressures except tunnel-wall static pressures were measured with strain-gage-type transducers and recorded on automatic balance potentiometers. The tunnel-wall static pressures were read on mercury manometers and recorded periodically during each test run.

Survey Procedures

At each of the downstream stations, one vertical and three horizontal surveys were made of the flow field. The vertical survey was made along the jet center line stepwise from the plate surface outward until a zero hydrogen concentration was obtained. Horizontal surveys were then made at points above the plate corresponding to maximum and half-maximum concentration and at a point midway between the plate surface and the point of maximum concentration. For each horizontal survey, the edge of the mixing region was located, and a stepwise survey was made across the flow field from this point until a hydrogen volume fraction of zero was obtained. At each point in the survey, a gas sample and a pitot-pressure measurement were taken.

Data Reduction and Accuracy

The pressure and concentration data at each survey point were reduced to yield values of mass fraction, mixture molecular weight, Mach number, mixture total and static temperature, velocity, mixture and air mass flux, and the hydrogen mass flow parameter. The molecular weight of the hydrogen-air mixture was computed by assuming molecular weights of the components of 2.016 and 29.0, respectively. Mixture total temperature was obtained from the mixture mass averaged total enthalpy computed from the measured total temperatures of the jet and free stream. The mixture was assumed to be a perfect gas and the values of Mach number, static temperature, and velocity computed using the equations for one-dimensional isentropic flow presented in reference 14. Local density of the mixture, used to compute the mass flux parameters, was calculated by using the ideal gas equation of state with the universal gas constant equal to 8.31 J/mol-K (1.986 cal/mol-K).

During the course of the tests, it was determined that the center line of the hydrogen-air flow field was not always coincident with the tunnel center line. This difference is believed to be a result of the small scale of the injector and probe tip and slight asymmetries of the tunnel flow. The maximum concentration was, therefore, sometimes obtained at a point to either side of the vertical survey location. The lateral location of the maximum concentration was taken as the center line of the mixing flow and the vertical survey was considered to have been made at a point slightly off center. In most cases, the distance between the tunnel and flow-field center lines $(y/d)_\alpha$ was less than one injector diameter. Probe position accuracy of the actuator mechanism for the vertical surveys was ± 0.127 mm, the same as the probe tip height. This value corresponds to a possible error in the vertical probe position of ± 0.125 injector diameter. Accuracy in the yaw mode was $\pm 0.10^\circ$ over a yaw angle range of less than $\pm 10^\circ$. At the widest survey location, the change in the x-position was less than two injector diameters. The gas chromatograph was periodically calibrated with 100-percent hydrogen from the supply line and the repeatability checked to a variation of less than one-half-percent full scale. The calibration of the instrument was nearly linear so that the error in any sample would be ± 0.005 volume fraction.

RESULTS AND DISCUSSION

Flow-Field Structure

The general structure of the flow field resulting from the normal injection is presented in figure 5. The data shown in figure 5 are profiles of hydrogen mass fraction taken on the tunnel center line and show trajectories of various concentrations. The hydrogen jet is quickly turned downstream by the free stream and mixes rapidly near

the jet, the maximum concentration decreasing to about 12-percent mass fraction in 7 injector diameters. Farther downstream, the mixing is slower, the maximum concentration decreasing to a mass fraction of 4 to 5 percent at an x/d of 60. The bow shock, determined from schlieren photographs, was not appreciably affected by a change in q_r and was essentially a Mach line downstream of an x/d of 20. Details in the vicinity of the injector were not clear from the present tests; however, flow details in this region are presented in references 6, 7, and 9 for thinner boundary layers and larger q_r than the present investigation.

The extent of the separation depends on the boundary-layer thickness relative to the injector diameter and the degree of underexpansion of the jet. From physical considerations of the injection disturbance, it may be reasoned that with a constant jet diameter, injection into a thick boundary layer will produce a greater absolute penetration near the jet, but the jet will be turned downstream somewhat before encountering the high velocity free stream and a weaker bow shock in the free stream will result. Therefore, the injector effective back pressure would be less.

For the free-stream conditions of figure 5, the minimum jet condition for sonic injection was a q_r of approximately 0.45. This value is equivalent to a jet exit static pressure and thus an effective back pressure of 0.63 atmosphere or approximately 40 percent of the free-stream pitot pressure. For these tests most of the jet penetration into the airstream occurs within 7 injector diameters, and the mixing region remains almost entirely embedded in the boundary layer. Variation of the static pressure vertically across the mixing region was less than 2 percent.

Jet Penetration

Although jet penetration has been discussed considerably in the literature, there are various definitions of penetration. As used herein, the term "penetration" is referred to the edge of the mixing region in the vertical center-line plane, where ν is 0.005, and is denoted as $(z/d)_0$; the height at which the concentration is maximum is referred to as "penetration to α_{\max} " and is denoted as $(z/d)_{\alpha}$. Figures 6 and 7 compare the present penetration data with various data correlations from the literature and illustrate the effect of the dynamic-pressure ratio at an x/d of 7 and the maximum concentration and penetration trajectories for a q_r of 1.0.

Correlations are presented in reference 9 for the penetration and α_{\max} trajectories and are given here for normal sonic injection of hydrogen in a Mach 4.03 free stream:

$$\left(\frac{z}{d}\right)_0 = 3.37(q_r)^{0.5} \left(\frac{x}{d}\right)^{0.0866} \quad (1)$$

$$\left(\frac{z}{d}\right)_\alpha = 3.45(q_r)^{0.533}\left(\frac{x}{d}\right)^{-0.259} \quad (2)$$

These equations were derived for data at x/d equal to or greater than 7. At an x/d of 7 (fig. 6), equation (1) underpredicts the penetration by about 20 percent and has a slope of 0.5 compared with 0.3 for a fairing of the experimental data. For a q_r of 1.0 (fig. 7), the penetration trajectory predicted by equation (1) is as much as 45 percent lower than the data at an x/d of 200. Based on measurement accuracy, the probable error of the data points has been estimated to be less than 0.2 injector diameter or approximately 3 percent. Equation (2), in figure 6, shows a reasonable agreement with the data and has a slope of 0.533 compared with 0.6 for a fairing of the data points. The α_{\max} trajectory given by equation (2), for a q_r of 1.0 (fig. 7), approaches the plate surface at large values of x/d whereas the data diverge.

Another correlation for the penetration of a normal jet, reported in reference 10 and given here for sonic injection into a Mach 4.03 free stream, is

$$\left(\frac{z}{d}\right)_0 = 3.40(q_r)^{0.392}\left(\frac{x}{d}\right)^{0.134} \quad (3)$$

Equation (3) was derived from data taken at free-stream Mach numbers of 1.6 and 3.0 over an x/d range of 14 to 167. Equation (3) is presented in figures 6 and 7 and gives a better prediction of the penetration than equation (1).

Also shown in figures 6 and 7 is the jet center-line trajectory (α_{\max} trajectory) in the near field calculated from the method of reference 9 in which the jet is considered as being composed of cylindrical elements of length $d\left(\frac{h}{d}\right)$ and the aerodynamic drag on each element is computed from empirical equations. The equation from reference 9 is

$$6.91q_r \int_{\theta}^{\theta_i} \frac{d\theta}{C_D(\theta) \sin^2 \theta} = \left(0.22 \frac{h}{d} + 2.25\right)^4 - 2.25^4 \quad (4)$$

where

$$C_D(\theta) = 1.2 + (M_\infty \sin \theta)^{7/2} \quad (0 \leq M_\infty \sin \theta \leq 1)$$

$$C_D(\theta) = 1.06 + 1.14(M_\infty \sin \theta)^{-3} \quad (M_\infty \sin \theta \geq 1)$$

Equation (4) underpredicts the effect of q_r on the penetration at an x/d of 7. The effect of boundary layer is not accounted for in equation (4); however, calculations made by using the mass-averaged boundary-layer conditions rather than free-stream conditions made no significant change in the trajectory or the effect of q_r .

Penetration Trajectories

Trajectories of maximum concentration, half-maximum concentration, and the penetration height are correlated with the ratio of jet dynamic pressure to free-stream dynamic pressure and are presented in figures 8(a), 8(b), and 8(c), respectively. During examination of the data, it was found that the maximum concentration trajectories had a minimum value that occurred farther downstream at the higher values of q_r . A factor $q_r^{-1.6}$ applied to the x/d coordinate produced the family of curves presented in figure 8(a). The turning of the maximum concentration trajectory beyond the parallel (that is, $\cong 90^\circ$) with the plate surface, as shown by the initial decrease in $(z/d)_\alpha$, is thought to be more evident than in previous tests because of the thick boundary layer. Minimum values of $(z/d)_\alpha$ occurred at values of x/d ranging from 9 to 45 for values of q_r between 0.5 and 1.5, respectively. Examination of the trajectories of the point at which the mass concentration is one-half the maximum led to a correlating factor of $q_r^{-0.8}$ which, when applied to the x/d coordinate, produced the family of curves similar to those for the maximum concentration, presented in figure 8(b). At all x/d stations, the penetration increased in proportion to the 0.3 power of the dynamic-pressure ratio. The correlated trajectories are presented in figure 8(c). For x/d less than 120, the data may be represented by the following equation:

$$\left(\frac{z}{d}\right)_\alpha = 3.87(q_r)^{0.300}\left(\frac{x}{d}\right)^{0.143} \quad (5)$$

This equation is similar to equation (3); the differences in the coefficient and exponents between equations (3) and (5) are probably due in part to the different injected gases and boundary-layer thicknesses.

Decay of Maximum Concentration

The concept of a potential core length has been used in reference 5 to nondimensionalize the longitudinal coordinate and to obtain a correlation of the maximum concentration decay with downstream distance. The potential core length x_0 is defined as the distance along the center line from the injector to the downstream station at which the concentration of the injected gas first decreases from 100 percent. For the present data, values of the potential core length, ranging between 0.14 and 0.25 injector diameter, were obtained by extrapolating the curves in figure 9(a) to a concentration of 100 percent and, therefore, must be considered as a correlating parameter rather than a true value of potential core length. Figure 9(b) presents the correlated maximum concentration decay data of the present investigation and includes the data for hydrogen from reference 5. The average deviation of the data from the correlated curve is less than 10 percent; the maximum deviation is 30 percent at an x/d of 7. The slope of the correlated curve for x/x_0 less than 200 is approximately -0.5. Coaxial data from reference 3 indicated a maximum

concentration decay inversely proportional to x^2 . Reference 5 presented a correlation for the potential core length for normal injection as a function of the molecular weight and the ratio of specific heats of the injected gas, and the ratio of jet mass flux to free-stream mass flux. For hydrogen injection, the correlation reduces to

$$\frac{x_0}{d_j} = 0.317\lambda^{0.54} \quad (6)$$

and is compared with the present data in figure 10. Note that in equation (6), x_0 is divided by the effective jet diameter d_j which is the injector diameter corrected by the injector discharge coefficient.

Profile Data

Nondimensional profiles of concentration, velocity, and total pressure for the vertical survey and the horizontal survey through the point of maximum concentration are presented in figures 11 to 13 and figures 14 to 16, respectively. The vertical concentration profiles in figure 11 are nondimensionalized and the origin of the coordinate system shifted to $(z/d)_{ref}$. Note that the vertical coordinate near the wall is nondimensionalized by a parameter different from that used above the point of peak concentration. The shape of the upper part of the profiles was not affected by q_r and could be represented by a Gaussian-type function of the form

$$\frac{\alpha}{\alpha_{ref}} = \exp \left\{ -5 \left[\frac{\left[\frac{z}{d} - \left(\frac{z}{d} \right)_{ref} \right]^{b_1}}{\left[\left(\frac{z}{d} \right)_0 - \left(\frac{z}{d} \right)_{ref} \right]} \right]^2 \right\} \quad (7)$$

where b_1 , the vertical profile shape index, is selected to give a reasonable fit with the data. At x/d stations, downstream of 30, the value of b_1 is constant at a value of 2.70; thus, it is suggested that the flow field has become fully developed. It has already been noted that the maximum concentration trajectory in figure 8 has a minimum near a value of $\left(\frac{x}{d} \right) q_r^{-1.6}$ of 30.

The section of the profiles at negative values of the vertical coordinate shows no systematic effect of q_r ; however, the variation of concentration across the profiles is, in general, less at lower q_r .

Nondimensional velocity profiles, in comparison with the undisturbed boundary-layer velocity at the injector station, are presented in figure 12. For each data profile, the value V_0 is the velocity at the edge of the mixing region at a height $(z/d)_0$ above the plate. Near the injector the peak velocity increases with increasing q_r because of

the direct increase of the mass flow rate of injected gas with q_r for constant free-stream conditions and a constant value of V_j . The initial ratio of jet velocity to free-stream velocity is approximately 2. At values of x/d downstream of 30, the shape of the velocity profiles approaches that of the boundary layer.

Nondimensional total-pressure profiles in the vertical plane are presented in figure 13 in comparison with the boundary-layer total-pressure profile. The total pressure at the edge of the mixing region generally increases with increasing x/d because of the addition to the mixing region of free-stream air that has passed through a weaker section of the bow shock. All the profiles exhibit approximately the same total-pressure loss due to the loss in momentum required to turn and accelerate the injected hydrogen. This region of low total pressure extends over approximately 60 percent of the vertical height of the flow field and is most severe at the upstream stations.

Nondimensional horizontal concentration profiles are presented in figure 14 with the lateral coordinate nondimensionalized by the average distance from the center line to each of the lateral edges of the mixing region $(\bar{y}/d)_0$. Values of $(\bar{y}/d)_0$ have a somewhat random variation of roughly 5 to 8 from an x/d of 7 to 200 with a ± 20 -percent deviation at a given station. It was found that the profile data could be represented by a Gaussian-type function of the form

$$\frac{\alpha}{\alpha_{\max}} = \exp \left\{ -5 \frac{\left[\frac{y}{d} - \left(\frac{y}{d} \right)_{\alpha} \right]^{b_2}}{\left[\left(\frac{y}{d} \right)_0 - \left(\frac{y}{d} \right)_{\alpha} \right]} \right\} \quad (8)$$

where b_2 is the horizontal profile slope index and takes on a value required to obtain a reasonable fit with the data.

Velocity profiles in the horizontal plane are presented in figure 15 and indicate a nearly uniform two-dimensional flow field downstream of about 60 injector diameters for q_r of 1.0. Corresponding total-pressure profiles, presented in figure 16, show a large variation in total pressure across the mixing region because of the changing density of the mixture. The pressure level near the center line never recovers from the injector disturbance and is less than 8 percent of free-stream total pressure. The static-pressure variation across the mixing region is less than 2 percent.

Flow-Field Contours

An indication of the overall accuracy of the profile data was obtained by comparing the integrated hydrogen mass flow rate with the metered hydrogen mass flow supplied to the jet. In terms of ξ , the ratio of integrated mass flow to jet mass flow $\dot{m}_{\text{int}}/\dot{m}_j$ is

$$\frac{\dot{m}_{int}}{\dot{m}_j} = \frac{4\xi_{max}A_o}{\pi d_j^2} \int_0^{1.0} \frac{\xi}{\xi_{max}} d\left(\frac{A}{A_o}\right) \quad (9)$$

and is presented in figure 17. Agreement of the integrated and metered mass flows improves as x/d increases and q_r decreases. This improvement is probably due to the smaller gradients in the concentration and velocity – which are associated with the local turbulence level – at the downstream stations and lower values of q_r . The characteristics of a binary gas flow field that affect the accuracy of concentration measurements are discussed in reference 3. For flow fields of this nature, differences between integrated and measured mass flow rates of 20 percent are considered to be typical.

The contours of hydrogen mass fraction, presented in figure 18, represent cross sections of the flow field in the YZ-plane and are bounded by the zero concentration contour. At x/d stations between 30 and 200 and for all values of q_r , the part of the contours above $(z/d)_\alpha$ may be represented by semicircles centered at $(z/d)_\alpha$. This representation suggests that the flow field above $(z/d)_\alpha$ is similar to coaxial mixing downstream of x/d of 30.

The air mass flow rate contours in the nondimensional form β/β_{max} and contained within the zero concentration contour are presented in figure 19. The mass flow rate of air contained within the mixing region was obtained by evaluating the integral

$$\dot{m}_1 = \beta_{max}A_o \int_0^{1.0} \frac{\beta}{\beta_{max}} d\left(\frac{A}{A_o}\right) \quad (10)$$

Results of the integrations were used to determine the average fuel-air ratio and the size of the undisturbed streamtube upstream of the injector that contains the same air mass flow rate as the mixing region. The undisturbed streamtube area A_1 was calculated for each x/d and q_r by assuming that it was of the same shape as A_o ; that is, the ratios of the height z to the average width $y = A/z$ of the undisturbed streamtube and the mixing region cross section were assumed to be equal. The height of the undisturbed streamtube z_1 was calculated from the continuity equation and the definition of boundary-layer displacement thickness:

$$z_1 = \frac{1}{2} \delta^* + \left[\left(\frac{1}{2} \delta^* \right)^2 + \frac{\dot{m}_1 z_o^2}{(\rho V)_\infty A_o} \right]^{1/2} \quad (11)$$

Values of z_1 obtained from equation (11) for the integrated air mass flows from equation (10) are given in the tables of figures 12 and 13. In application to the design of supersonic combustors, the size and shape of the undisturbed streamtube provide

information as to the spacing of injectors and the injector size to obtain penetration to the combustor centerline. If it is assumed that injection is from opposite walls and that a stoichiometric value of \bar{f} is desired, the combustor entrance must have a half-height equal to the value of z_1 that corresponds to the x/d station at which a stoichiometric average fuel-air ratio was obtained. Confining the flow field by the addition of an opposite wall or by the addition of adjacent injectors would be expected to change the mixing rate and penetration from that presented herein but would yield a stoichiometric average fuel-air ratio. The injector spacing is the average width of the undisturbed streamtube y_1 . An estimation of these parameters is discussed in the next section.

Estimation of Cold Flow Mixing Parameters

The mixing length relative to the combustor entrance height and the injector spacing required to give a stoichiometric average fuel-air ratio ($\bar{f} = 0.0293$ for hydrogen in air) have been estimated by superimposing the flow-field cross sections of single injectors. A schematic for a two-dimensional configuration with staggered injection from both walls is presented in figure 20. Injector spacing was selected so that the half-maximum concentration contour of the single jet flow field was approximately coincident with the half-maximum concentration contour of the adjacent and opposite injectors. With this choice of spacing the air mass flow that mixes with the hydrogen from one injector is contained within the half- α_{\max} contour, since the area bounded by the adjacent contours covers the entire cross section of the combustor. By denoting the area contained by the half- α_{\max} contour as A_5 , equation (10) for the air mass flow becomes

$$\dot{m}_1 = \beta_{\max} A_5 \int_0^{1.0} \frac{\beta}{\beta_{\max}} d\left(\frac{A}{A_5}\right) \quad (12)$$

The height of the confined air streamtube is given by equation (11) by replacing A_0 and z_0 with A_5 and z_5 , respectively.

Values of average fuel-air ratio obtained from the total injected hydrogen mass flow and the integrated air mass flow for the unconfined jet (eq. (11)), and the α/α_{\max} of 0.5 contour (eq. (12)) are presented in figure 21 as a function of x/d_j and q_r . The effect of q_r on the decay of \bar{f} for both conditions was found to be such that a factor of $q_r^{-1/2}$ provided a reasonable correlation. For the unconfined jet, the value of \bar{f}_0 is below stoichiometric for all x/d stations considered. Downstream of 30 injector diameters, the decay of \bar{f}_0 is inversely proportional to approximately $x/d_j^{0.6}$. For the case of simulated opposite wall injection, the average fuel-air ratio \bar{f}_5 is considerably higher than \bar{f}_0 and becomes stoichiometric at an x/d_j of about 200 for a q_r of 1.0. It is apparent that the lowest value of q_r will provide a stoichiometric average fuel-air ratio in the shortest distance. Also, using a coincident concentration contour

with a value less than half maximum would yield a stoichiometric value of \bar{f} at a shorter x/d since the resulting curve for the decay of \bar{f} would lie somewhere between the curves for \bar{f}_0 and \bar{f}_5 . However, the uniformity of the flow field would need to be investigated to select the optimum value.

To determine the combustor size, the average fuel-air ratio of the simulated combustor flow field is plotted in figure 22 as a function of x/z_1 . The value of z_1 represents the combustor entrance half-height. From figure 22, \bar{f}_5 is stoichiometric at a value of x/z_1 of approximately 40. The hydraulic diameter of a two-dimensional duct is twice the duct height or $4z_1$. The mixing length required for a stoichiometric average fuel-air ratio is approximately 10 hydraulic diameters which agrees with rule-of-thumb values sometimes considered for engine design. For a q_r of 0.5, the value of z_1 for a stoichiometric value of \bar{f}_5 is approximately 3.3 injector diameters – corresponding to an x/d_j of 140 from figure 21. The value of y_1 , which is the required injector spacing, corresponding to these conditions is approximately 3.0 injector diameters. The analysis just described is of interest in illustrating trends and general magnitudes; however, the numerical data values cannot be expected to apply directly to scramjet combustor design.

CONCLUDING REMARKS

An investigation of the penetration and mixing of hydrogen gas injected normal to a Mach 4.03 airstream from a sonic injector has been conducted for ratios of jet dynamic pressure to free-stream dynamic pressure q_r of 0.5 to 1.5. A correlation provided the best agreement with the present data (which correlated as a function of the 0.3 power of q_r) whereas other correlations underpredicted the effect of q_r . Differences between the present data and data correlations in the literature are probably due, in part, to the relatively thick boundary layer used in this investigation.

The decay of the maximum concentration, correlated with the potential core length parameter, was inversely proportional to approximately the square root of downstream distance at locations less than 50 injector diameters. Values of the potential core length agreed well with a correlation which gave the potential core proportional to the 0.54 power of the ratio of jet mass flux to free-stream mass flux.

Examination of the nondimensional concentration profiles on the vertical center line suggest that the profile shape above the point of maximum concentration is not dependent on the dynamic-pressure ratio and may be represented by a Gaussian-type function. The profiles show similarity at values of the downstream distance x/d equal to or greater than 60. Horizontal concentration profiles through the point of maximum concentration are also represented by a Gaussian-type function and exhibit similarity at values of x/d less than 60.

The loss in momentum and total pressure of the airstream caused by turning and accelerating the hydrogen jet resulted in an extensive region of very low total pressure. The region extended over 60 percent of the mixing region height near the center of the flow field and 30 percent of the mixing region width with a total pressure less than 8 percent of the free stream.

The results obtained from the present data were used to simulate staggered opposite-wall injection in a two-dimensional supersonic combustor by superimposing the single jet flow fields. An estimation of the cold flow mixing parameters indicated that the mixing length required for a stoichiometric average fuel-air ratio was approximately 10 hydraulic diameters.

Langley Research Center,
National Aeronautics and Space Administration,
Hampton, Va., January 5, 1971.

REFERENCES

1. Henry, J. R.; and McLellan, C. H.: The Air-Breathing Launch Vehicle for Earth-Orbit Shuttle - New Technology and Development Approach. Paper presented at AIAA Advanced Transportation Meeting, Cocoa Beach, Florida, Feb. 1970.
2. Povinelli, Louis A.; Povinelli, Frederick P.; and Hersch, Martin: A Study of Helium Penetration and Spreading in a Mach 2 Airstream Using a Delta Wing Injector. NASA TN D-5322, 1969.
3. Eggers, James M.; and Torrence, Marvin G.: An Experimental Investigation of the Mixing of Compressible-Air Jets in a Coaxial Configuration. NASA TN D-5315, 1969.
4. Torrence, Marvin G.: Concentration Measurements of an Injected Gas in a Supersonic Stream. NASA TN D-3860, 1967.
5. Torrence, Marvin G.: Effect of Injectant Molecular Weight on Mixing of a Normal Jet in a Mach 4 Airstream. NASA TN D-6061, 1971.
6. Zukoski, Edward E.; and Spaid, Frank W.: Secondary Injection of Gases Into a Supersonic Flow. AIAA J., vol. 2, no. 10, Oct. 1964, pp. 1689-1696.
7. Spaid, F. W.; Zukoski, E. E.; and Rosen, R.: A Study of Secondary Injection of Gases Into a Supersonic Flow. Tech. Rep. No. 32-834, Jet Propulsion Lab., California Inst. Technol., Aug. 1, 1966.
8. Vranos, Alexander; and Nolan, James J.: Supersonic Mixing of Helium and Air. Bumblebee Rept. No. TG 63-53, Appl. Phys. Lab., Johns Hopkins Univ., June 1964, pp. 131-161.
9. Orth, R. C.; Schetz, J. A.; and Billig, F. S.: The Interaction and Penetration of Gaseous Jets in Supersonic Flow. NASA CR 1386, 1969.
10. Faucher, Joseph E., Jr.; Goldstein, Sidney; and Tabach, Edward: Supersonic Combustion of Fuels Other Than Hydrogen for Scramjet Application. AFAPL-TR-67-12, U.S. Air Force, Feb. 1967.
11. Henry, J. R.; Andrews, E. H., Jr.; Pinckney, S. Z.; and McClinton, C. R.: Boundary Layer and Starting Problems on a Short Axisymmetric Scramjet Inlet. Compressible Turbulent Boundary Layers, NASA SP-216, 1968, pp. 481-508.
12. Jeffery, P. G.; and Kipping, P. J.: Gas Analysis by Gas Chromatography. Macmillan Co., c.1964.

13. Harris, Walter E.; and Habgood, Henry W.: Programmed Temperature Gas Chromatography. John Wiley & Sons, Inc., c.1966.
14. Anon.: Equations, Tables, and Charts for Compressible Flow. NACA Rep. 1135, 1953.

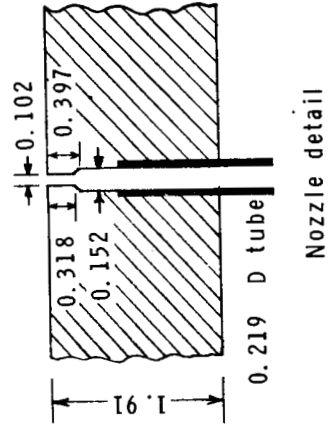
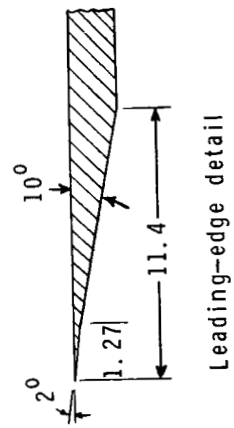
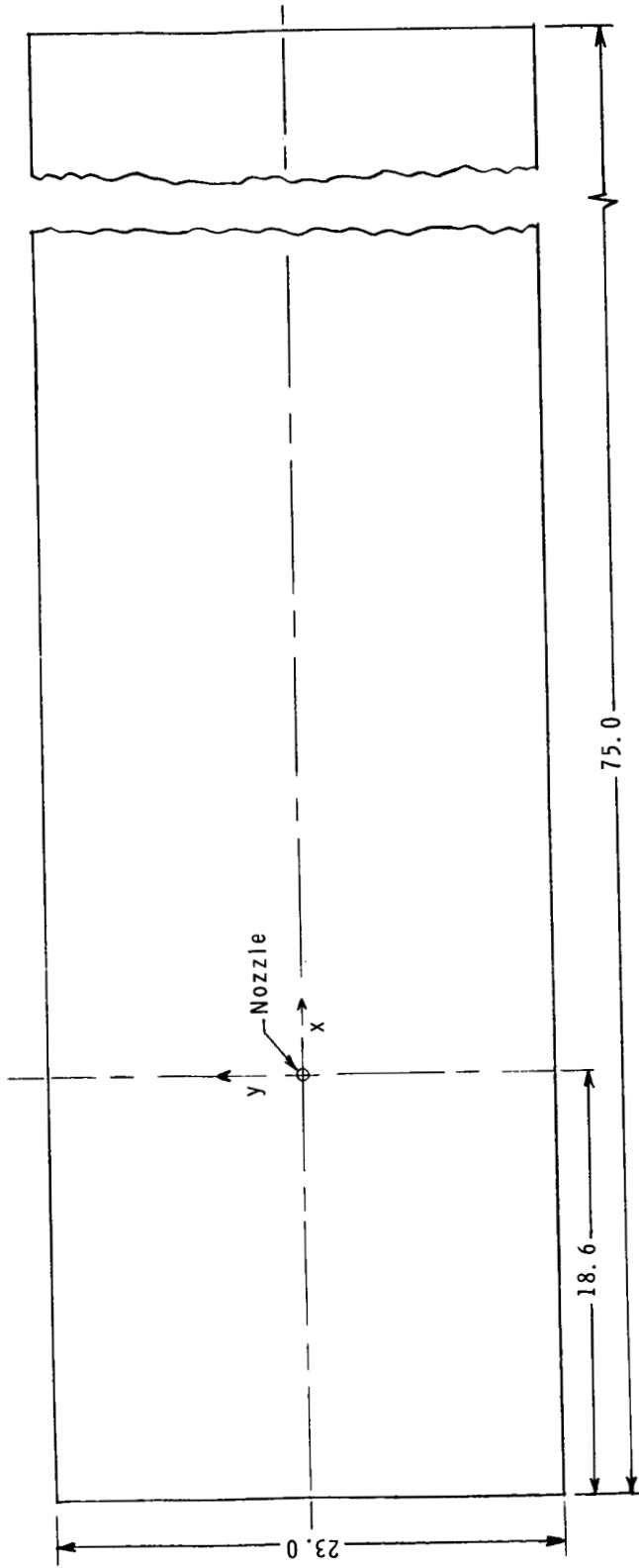


Figure 1.- Sketch of model. All linear dimensions are in centimeters.

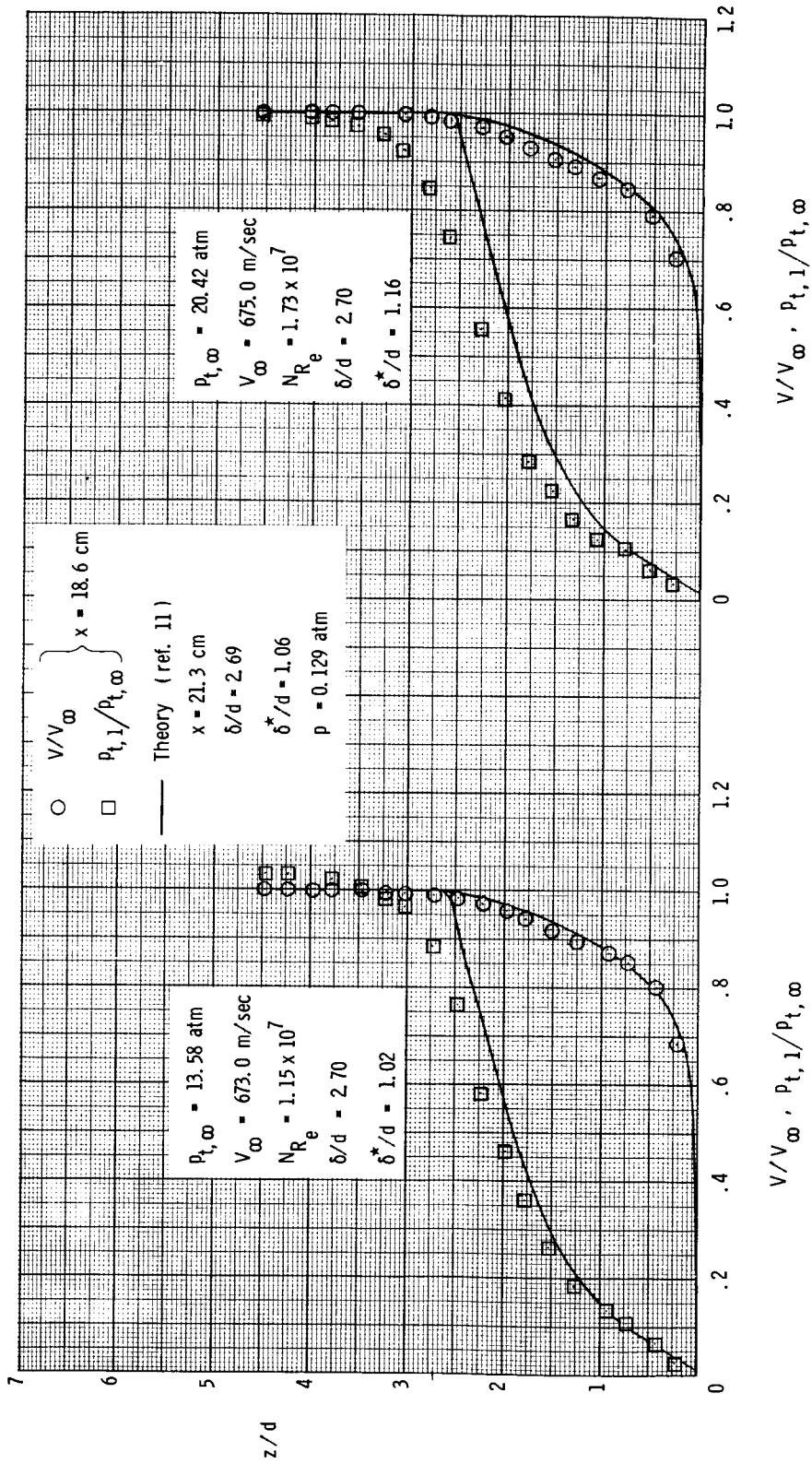


Figure 2.- Boundary-layer surveys on flat-plate model at injector exit station. No injection; T = 300 K.

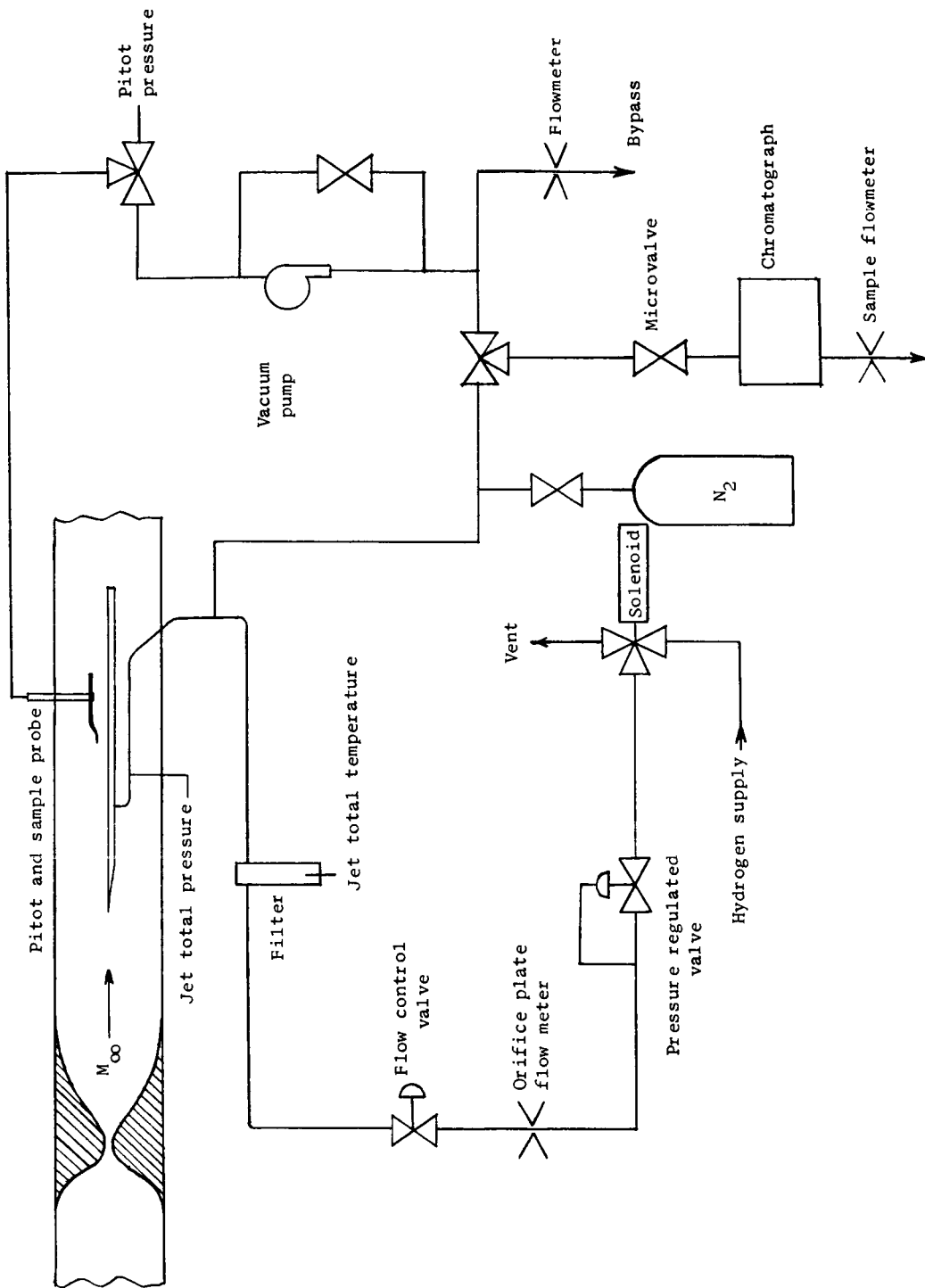


Figure 3.- Tunnel and injector flow schematic.

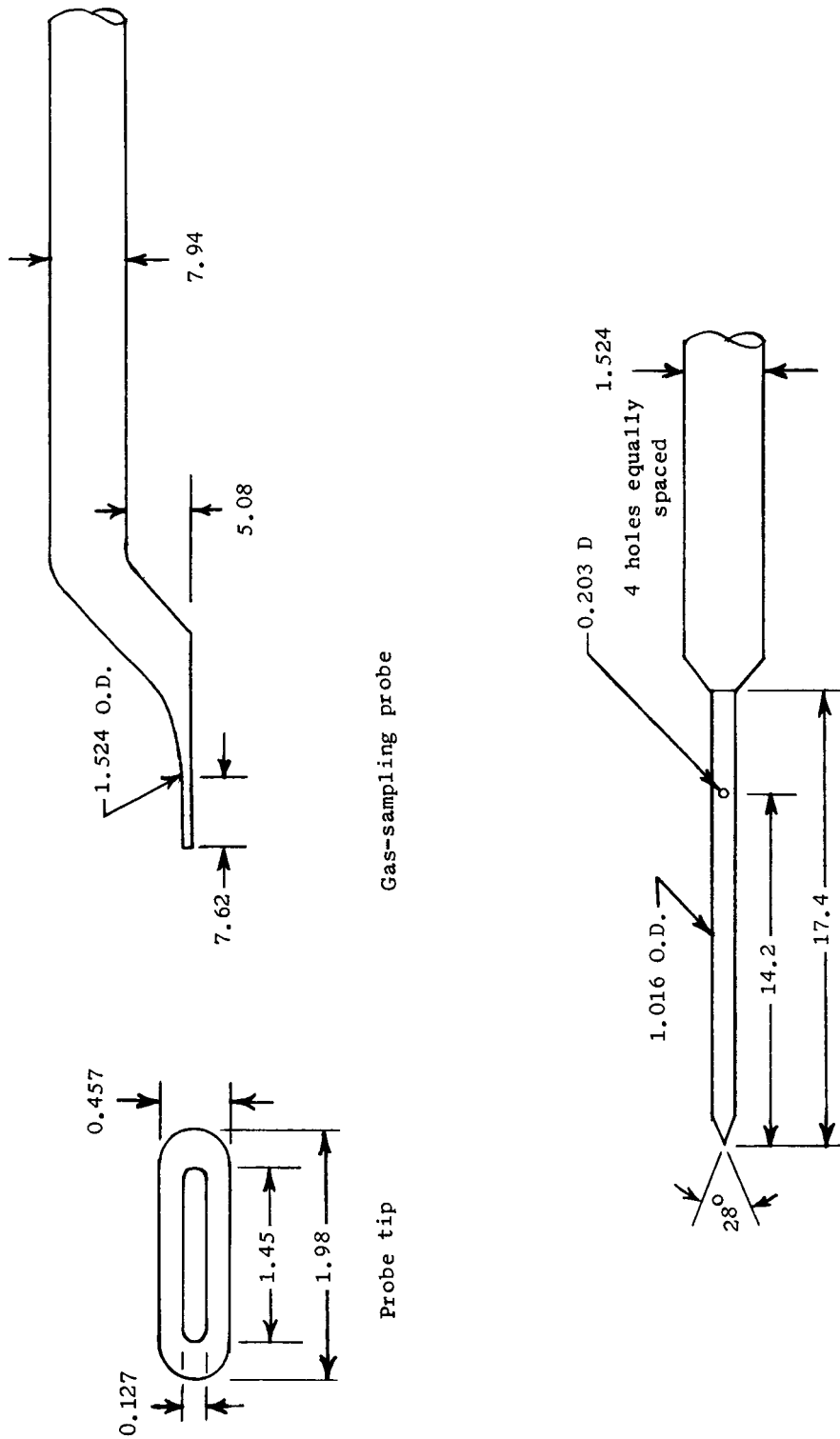


Figure 4.- Survey-probe design. All linear dimensions are in millimeters.

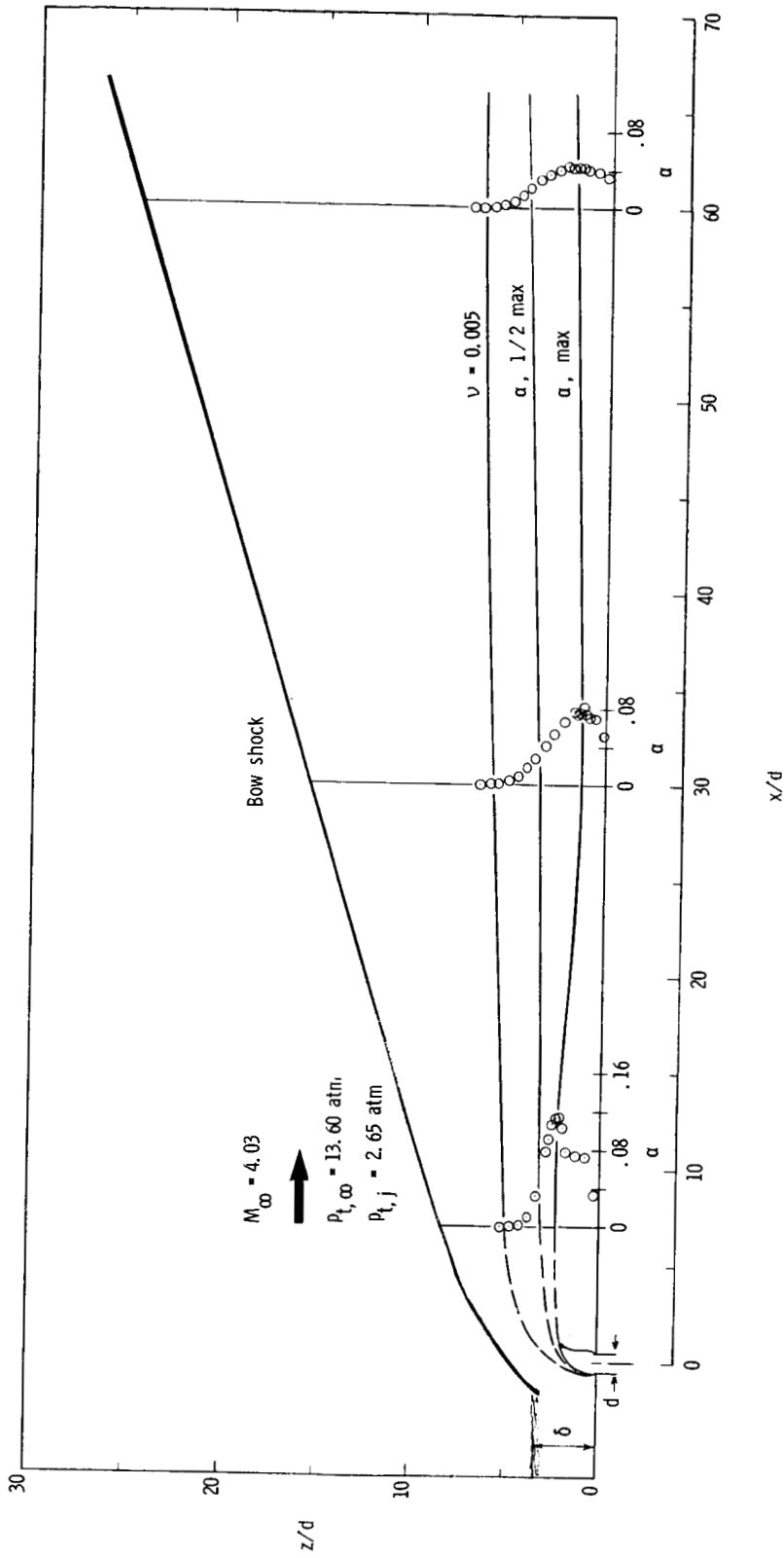


Figure 5.- Structure of flow field and mixing region. $q_r = 1.0$.

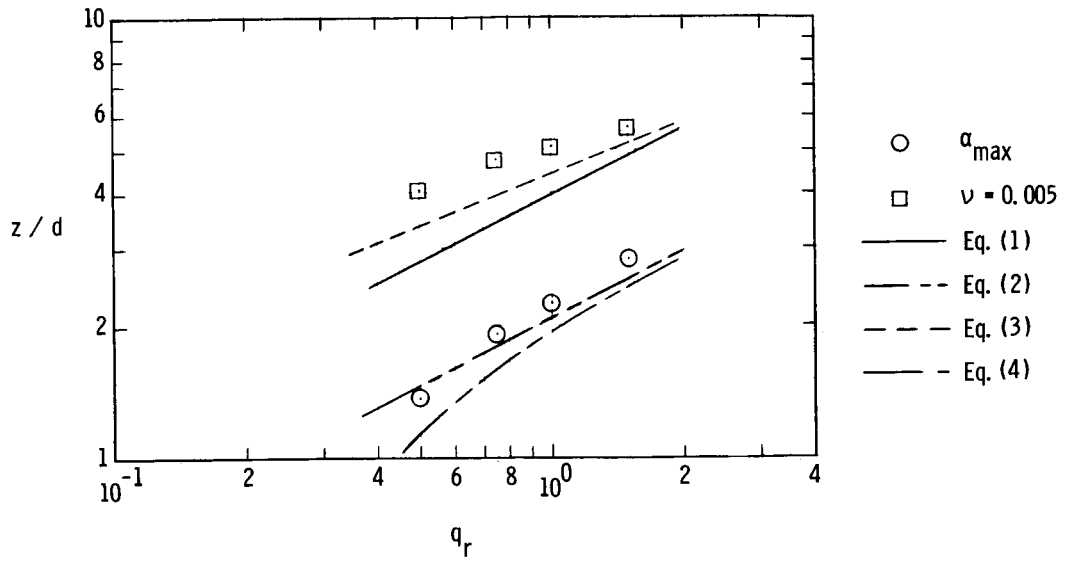


Figure 6.- Effect of dynamic-pressure ratio on the jet penetration.
 $x/d = 7$; comparison of data and correlations.

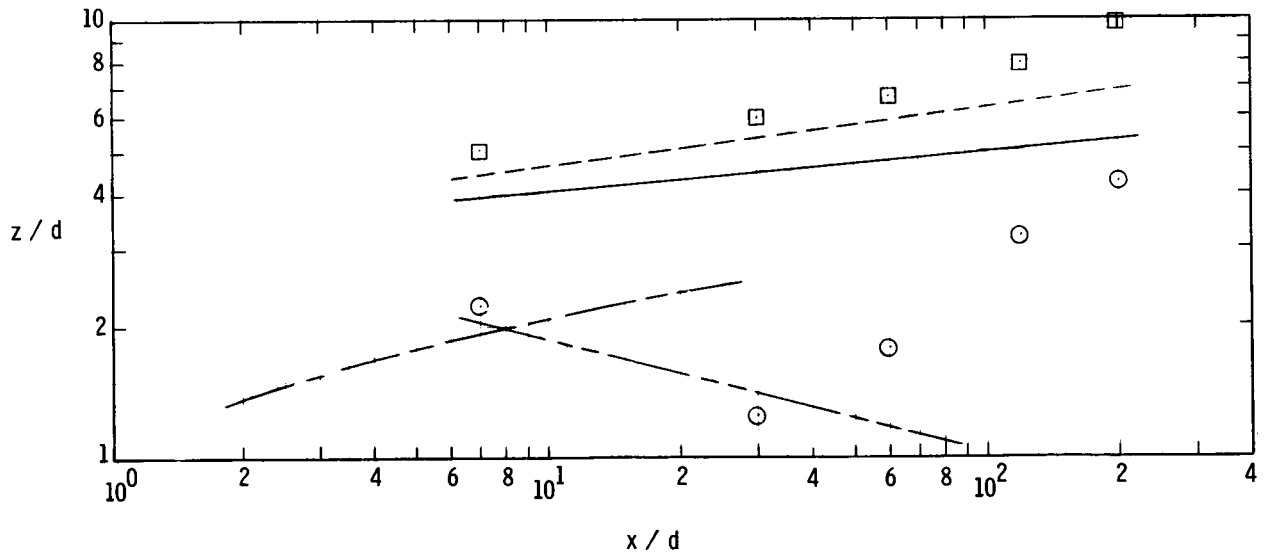
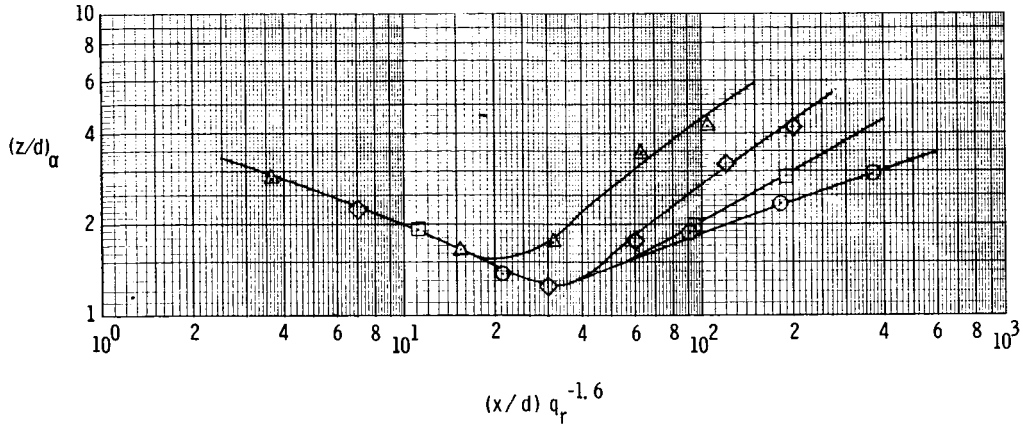
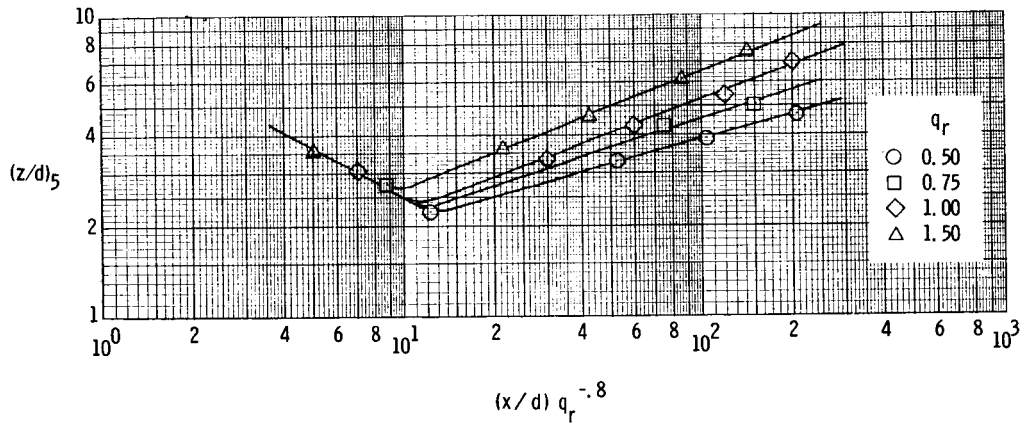


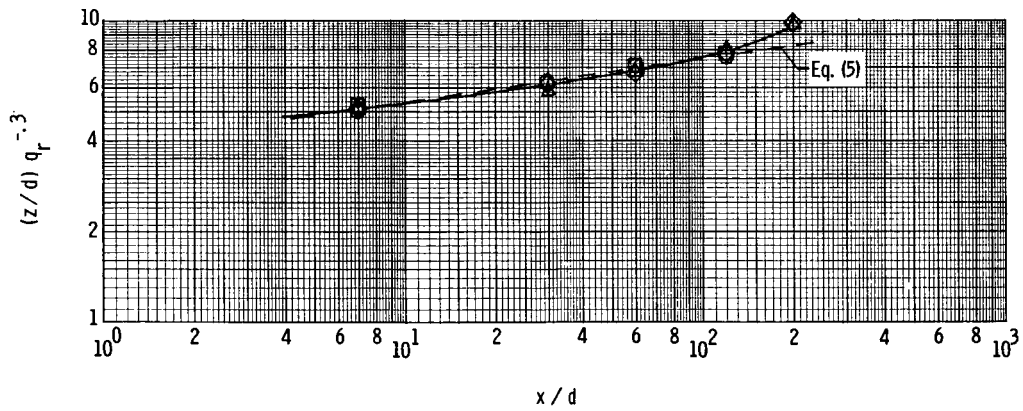
Figure 7.- Maximum concentration and penetration trajectories.
 $q_r = 1.0$; comparison of data and correlations.



(a) Maximum concentration trajectory.

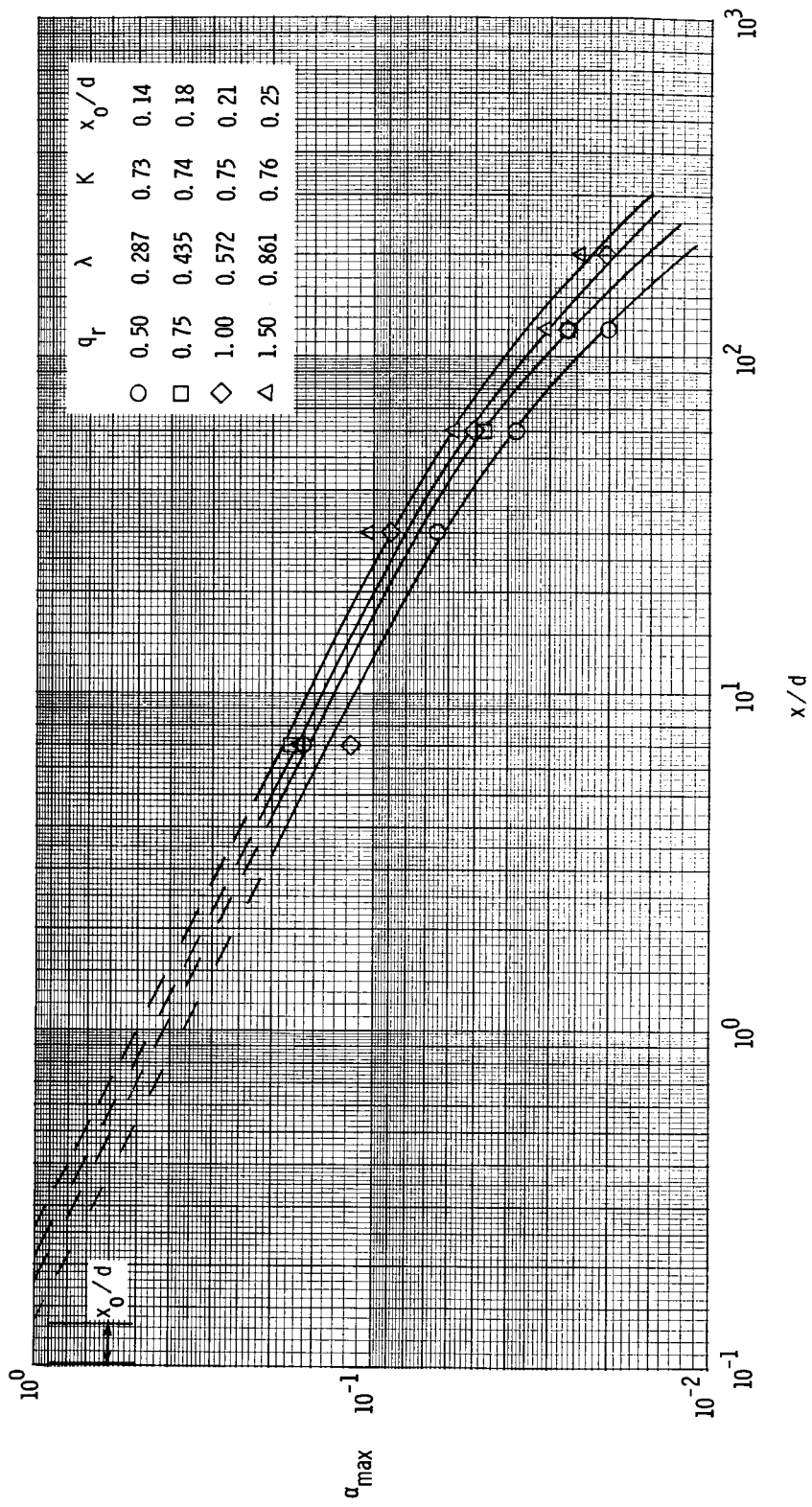


(b) Half-maximum concentration trajectory.



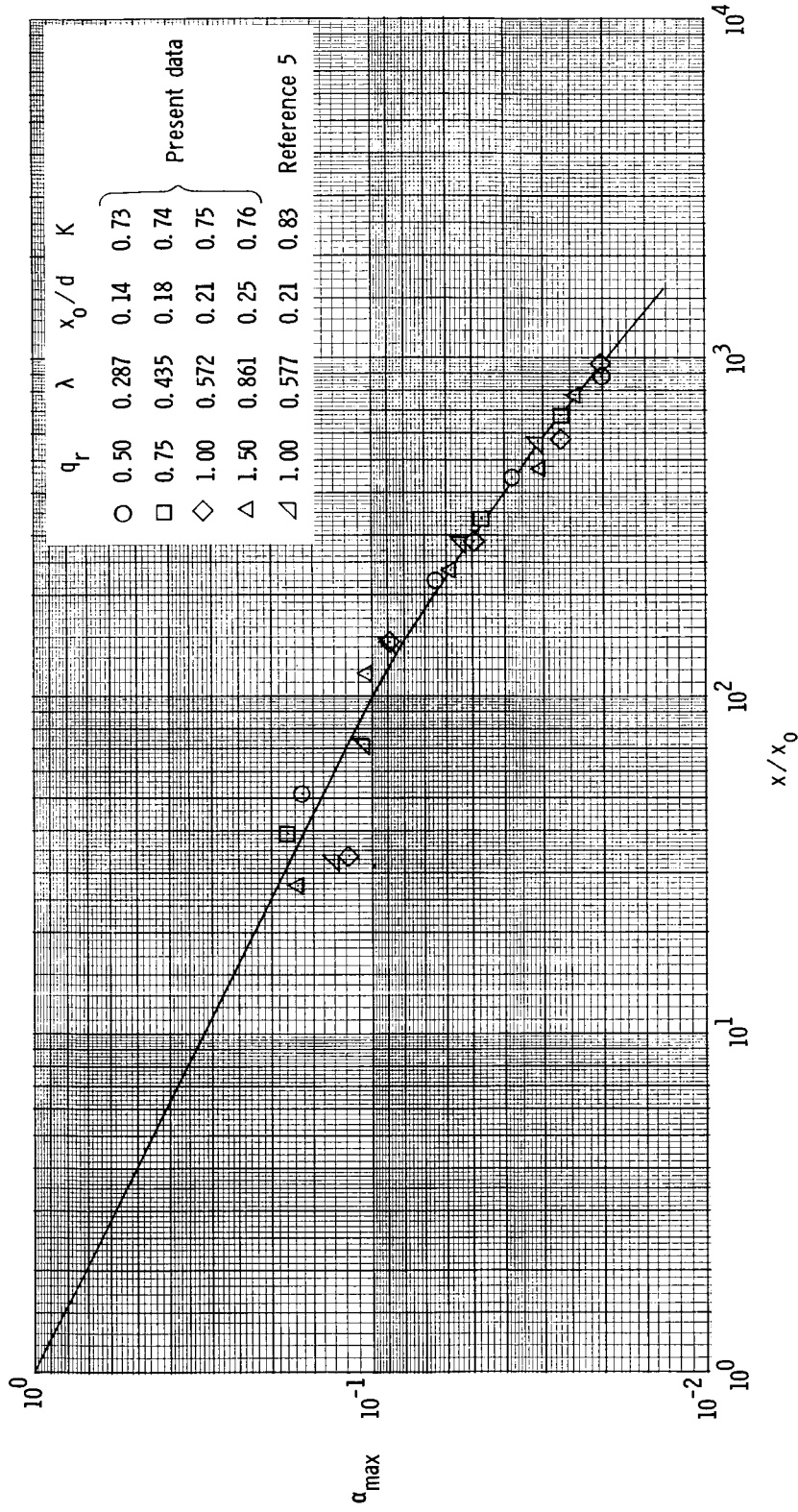
(c) Penetration trajectory; $\nu = 0.005$.

Figure 8. - Effect of dynamic-pressure ratio on penetration trajectories.



(a) Effect of dynamic-pressure ratio.

Figure 9. - Decay of maximum concentration with downstream distance.



(b) Correlated with potential core length.

Figure 9. - Concluded.

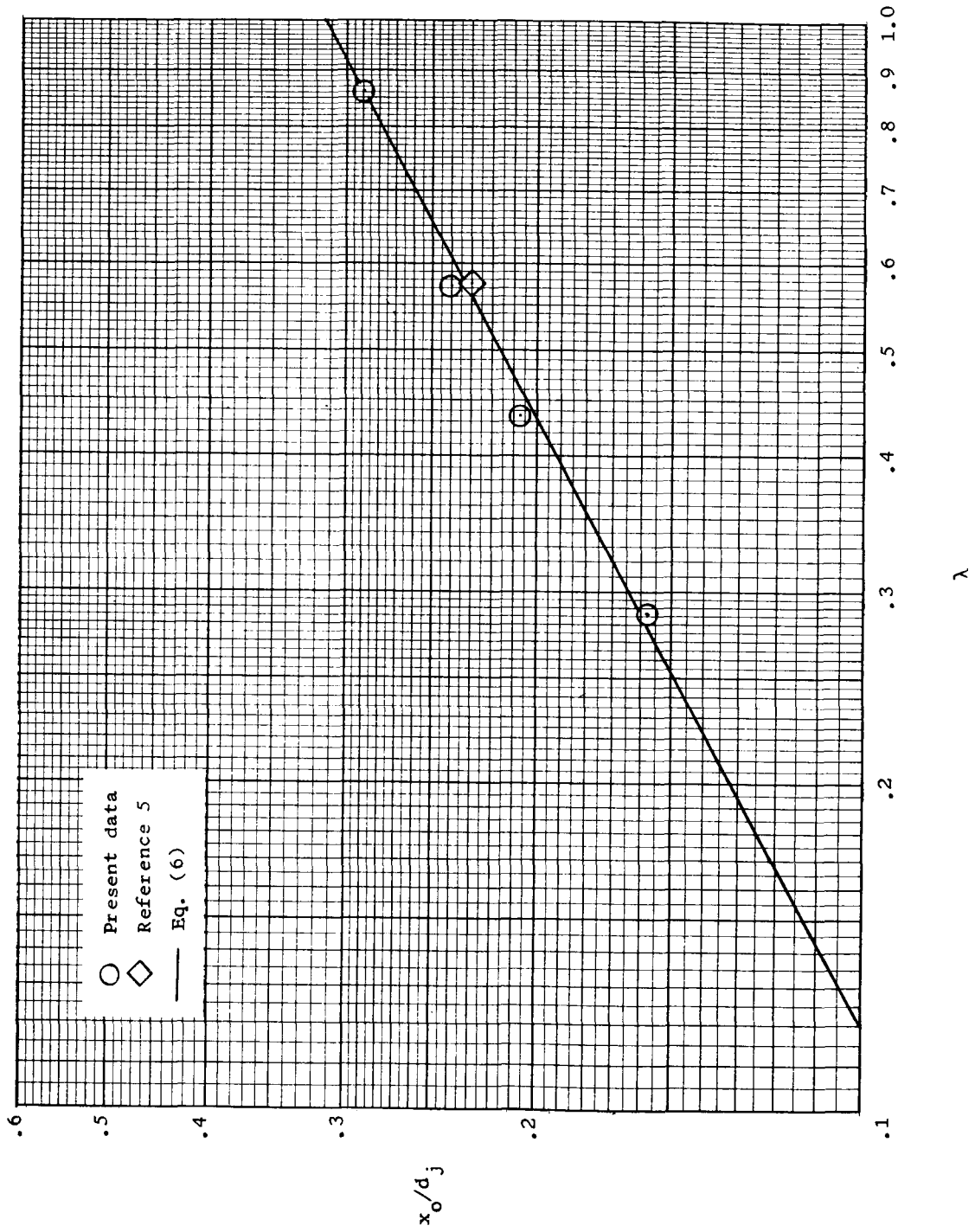
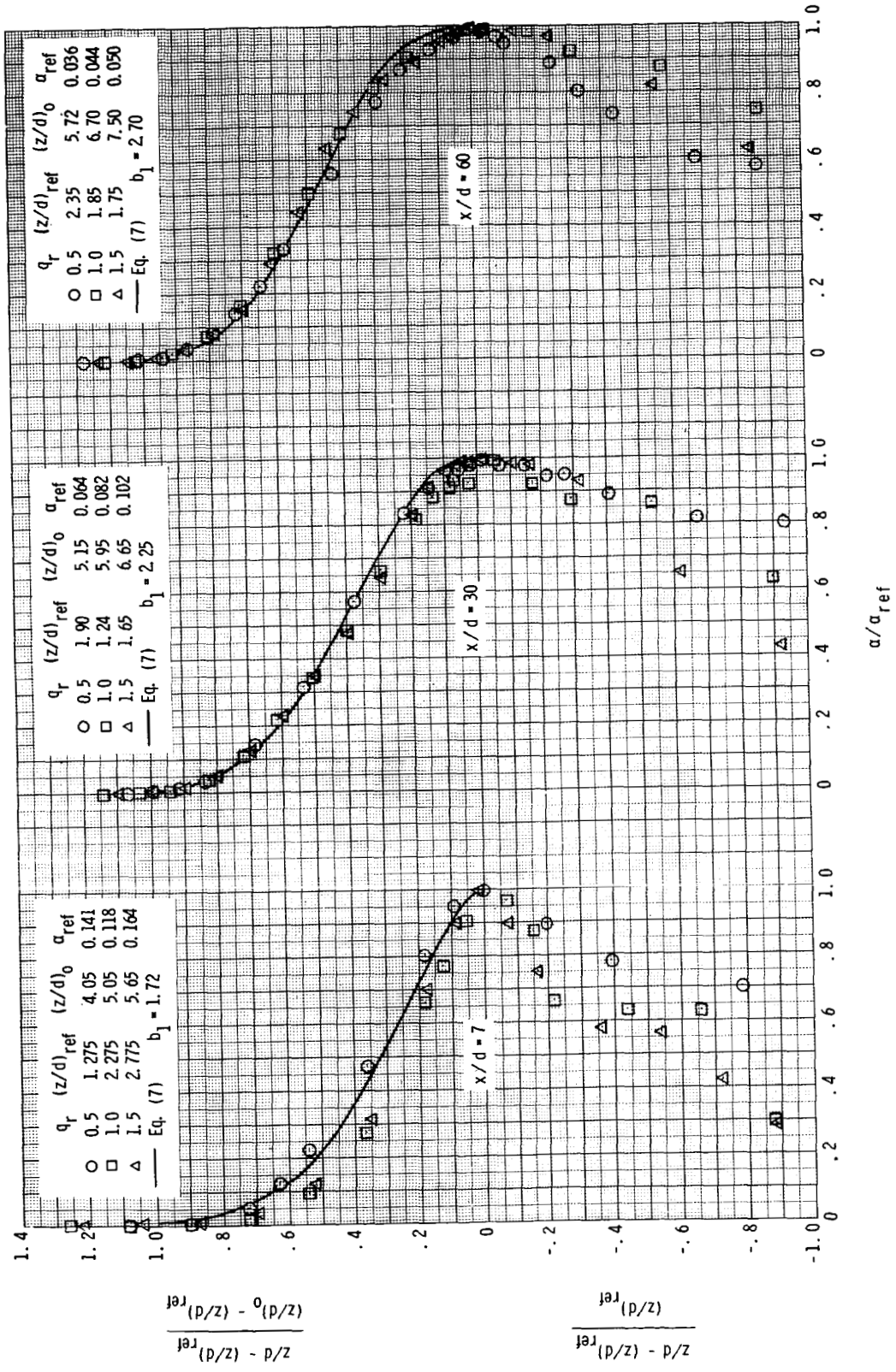
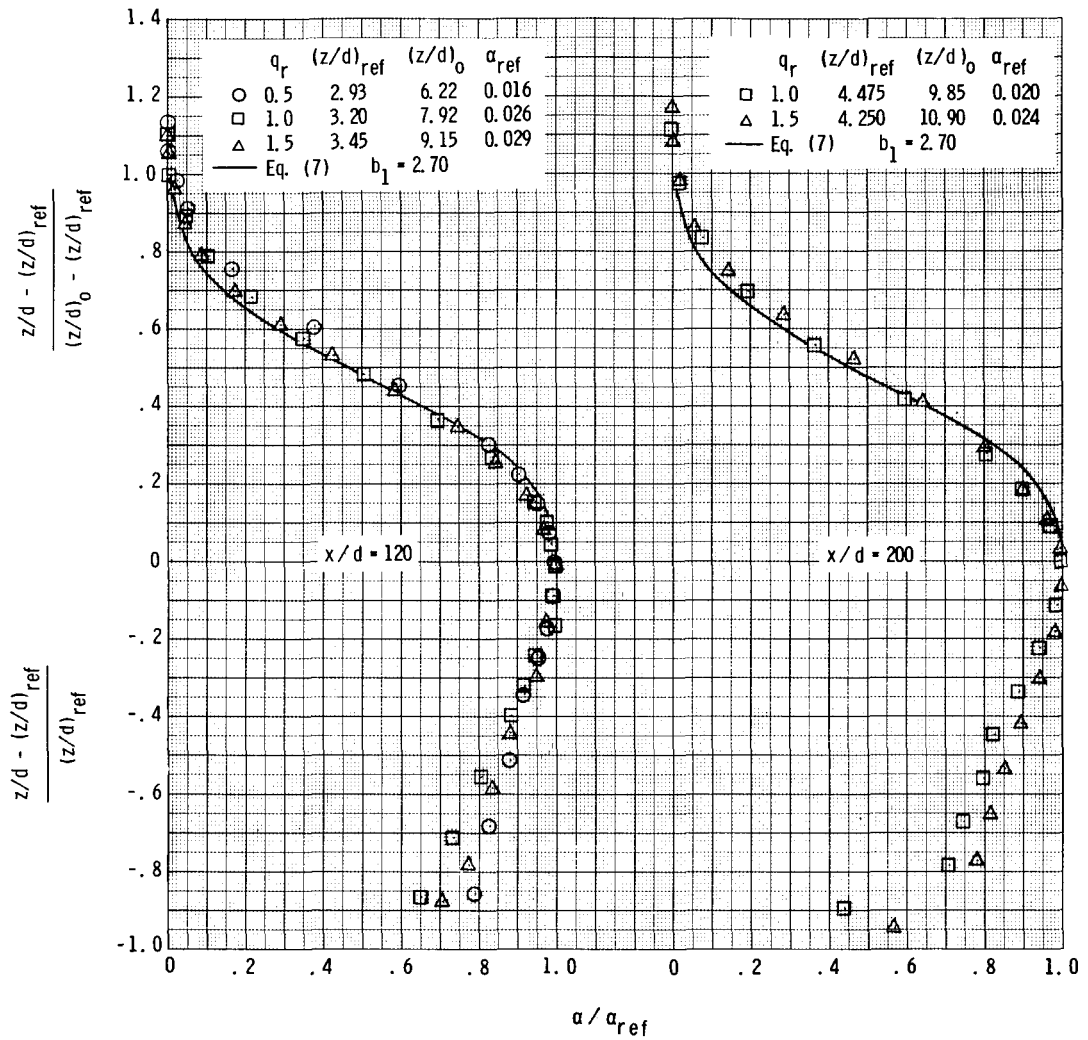


Figure 10.- Variation of potential core-length correlation parameter with mass flux ratio.

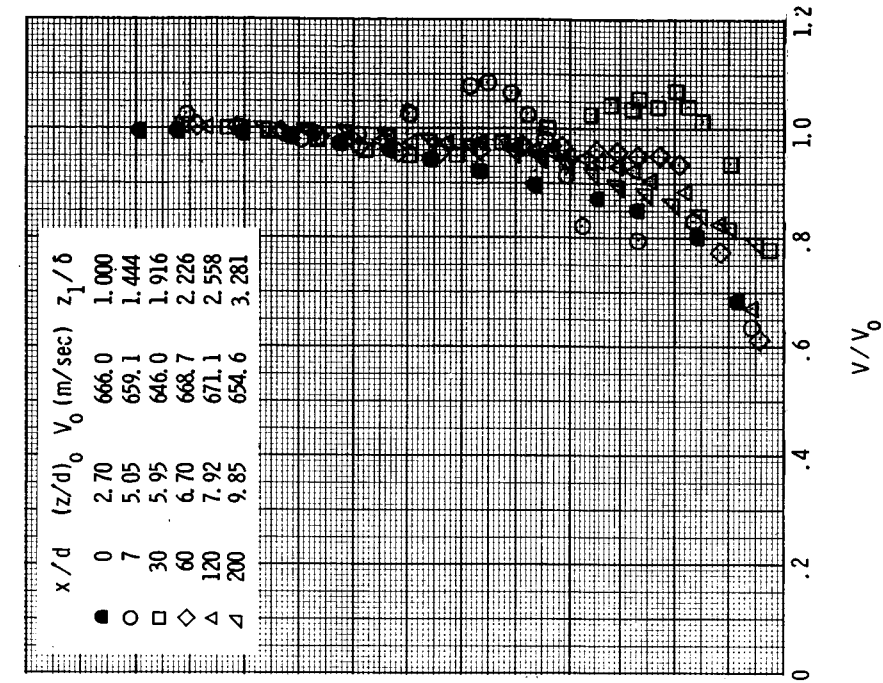


(a) $x/d = 7, 30, \text{ and } 60$.
 Figure 11. - Nondimensional concentration profiles. Vertical survey.

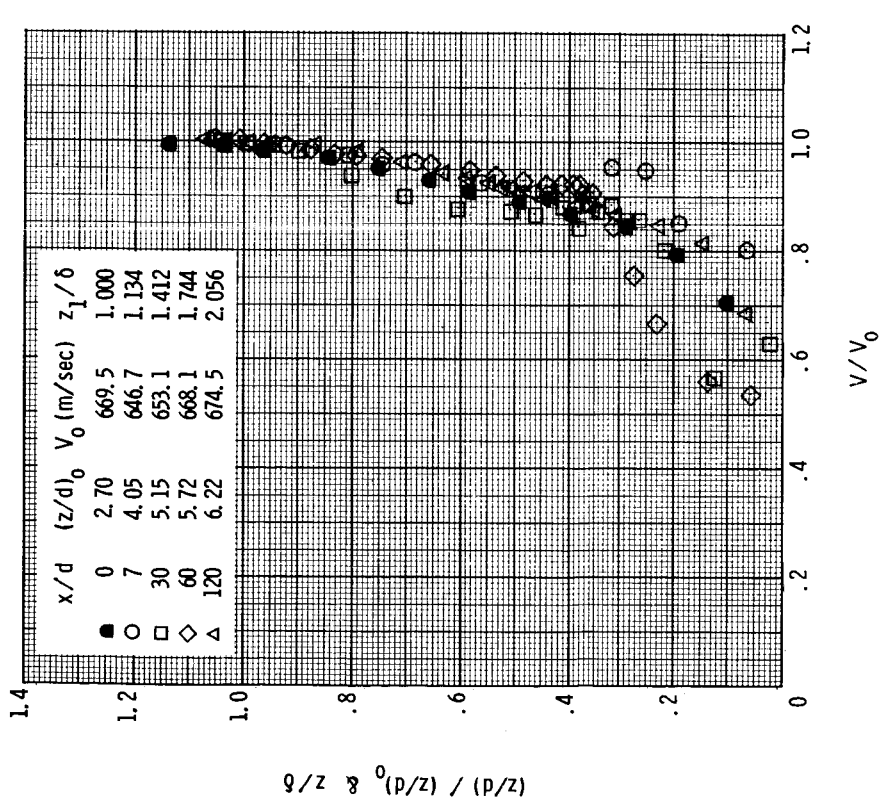


(b) $x/d = 120$ and 200 .

Figure 11. - Concluded.

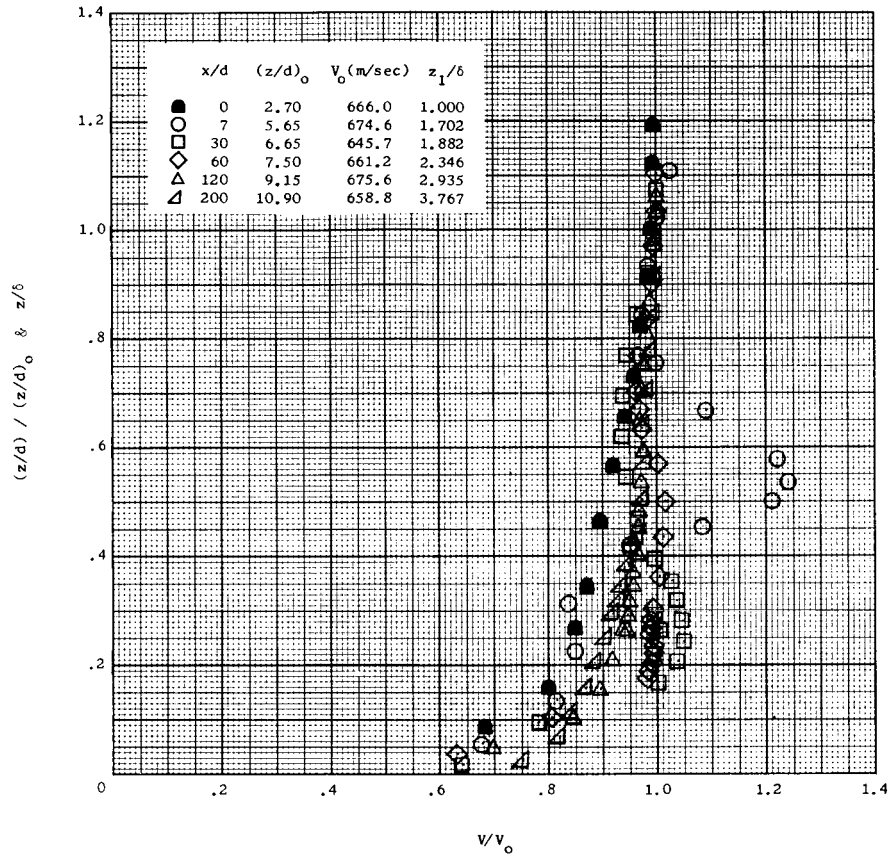


(a) $q_r = 0.5$.



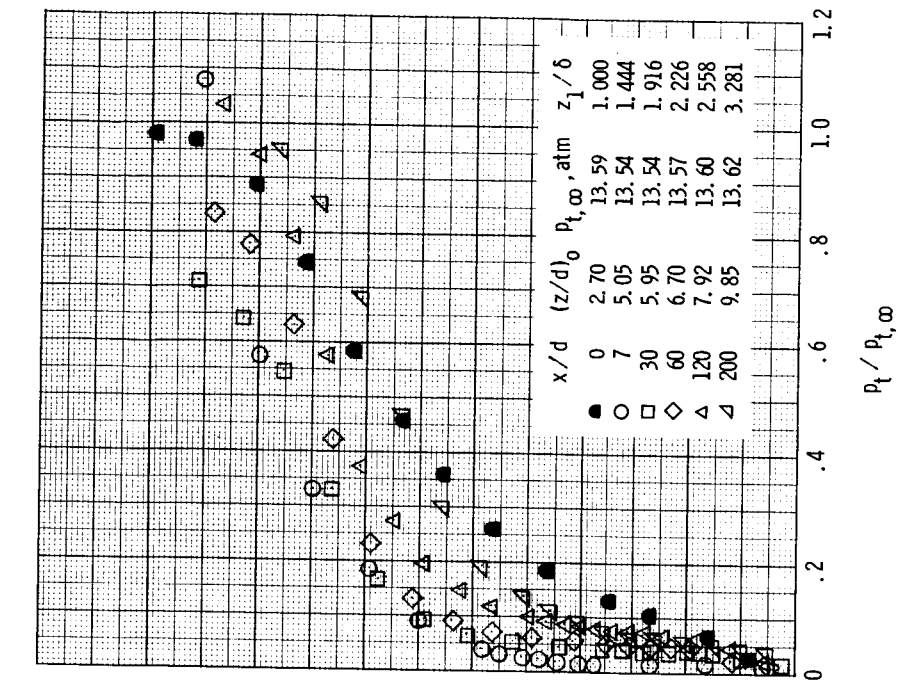
(b) $q_r = 1.0$.

Figure 12.- Nondimensional velocity profiles. Vertical survey.

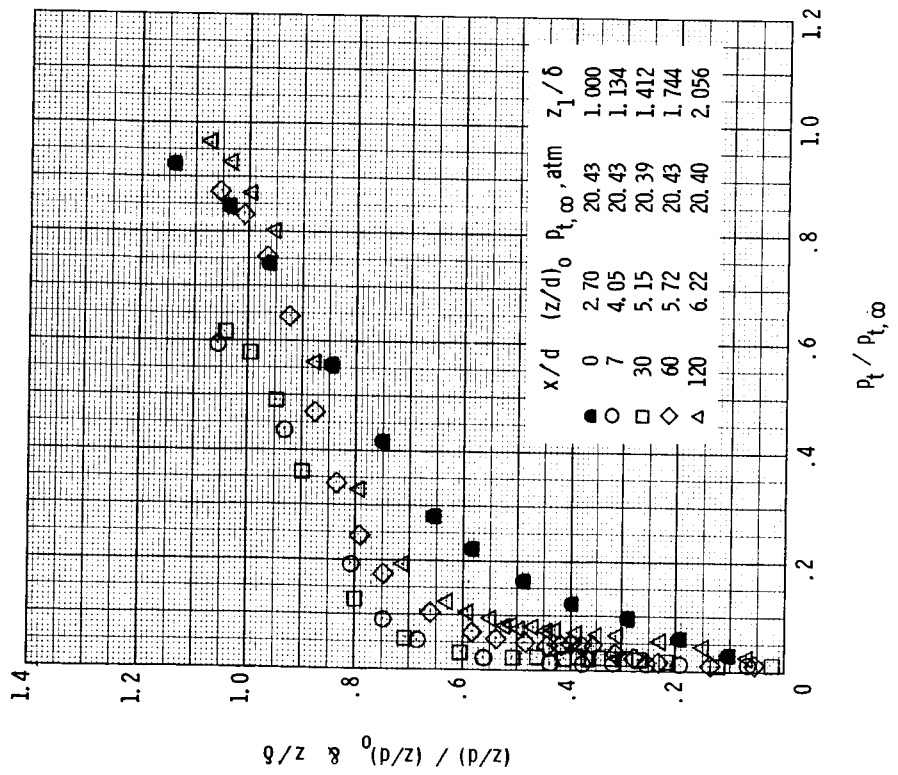


(c) $q_r = 1.5$.

Figure 12.- Concluded.

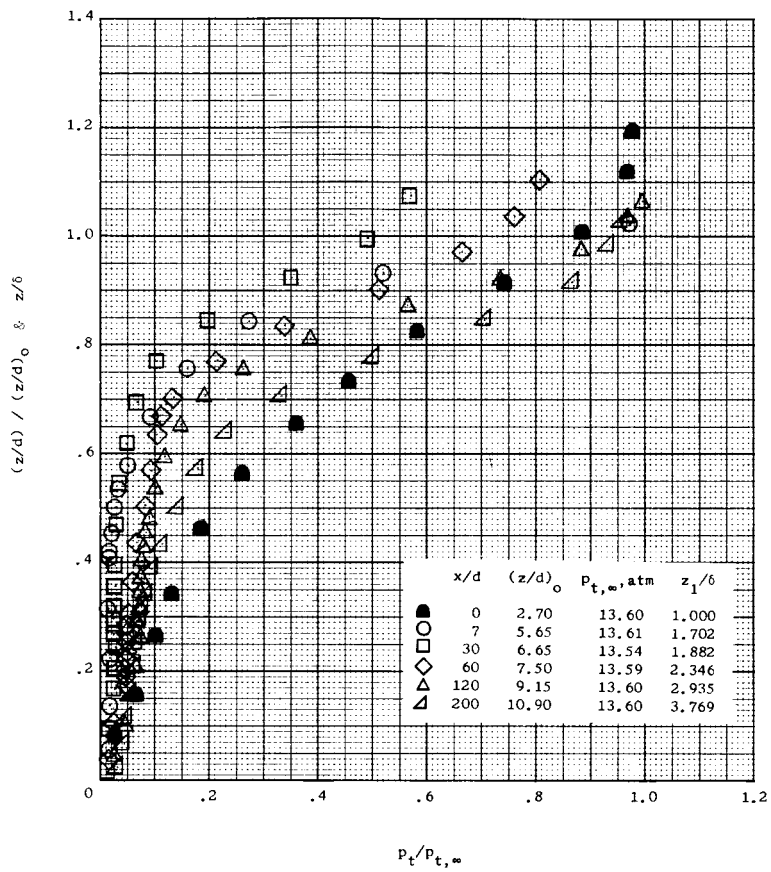


(a) $q_r = 0.5$.



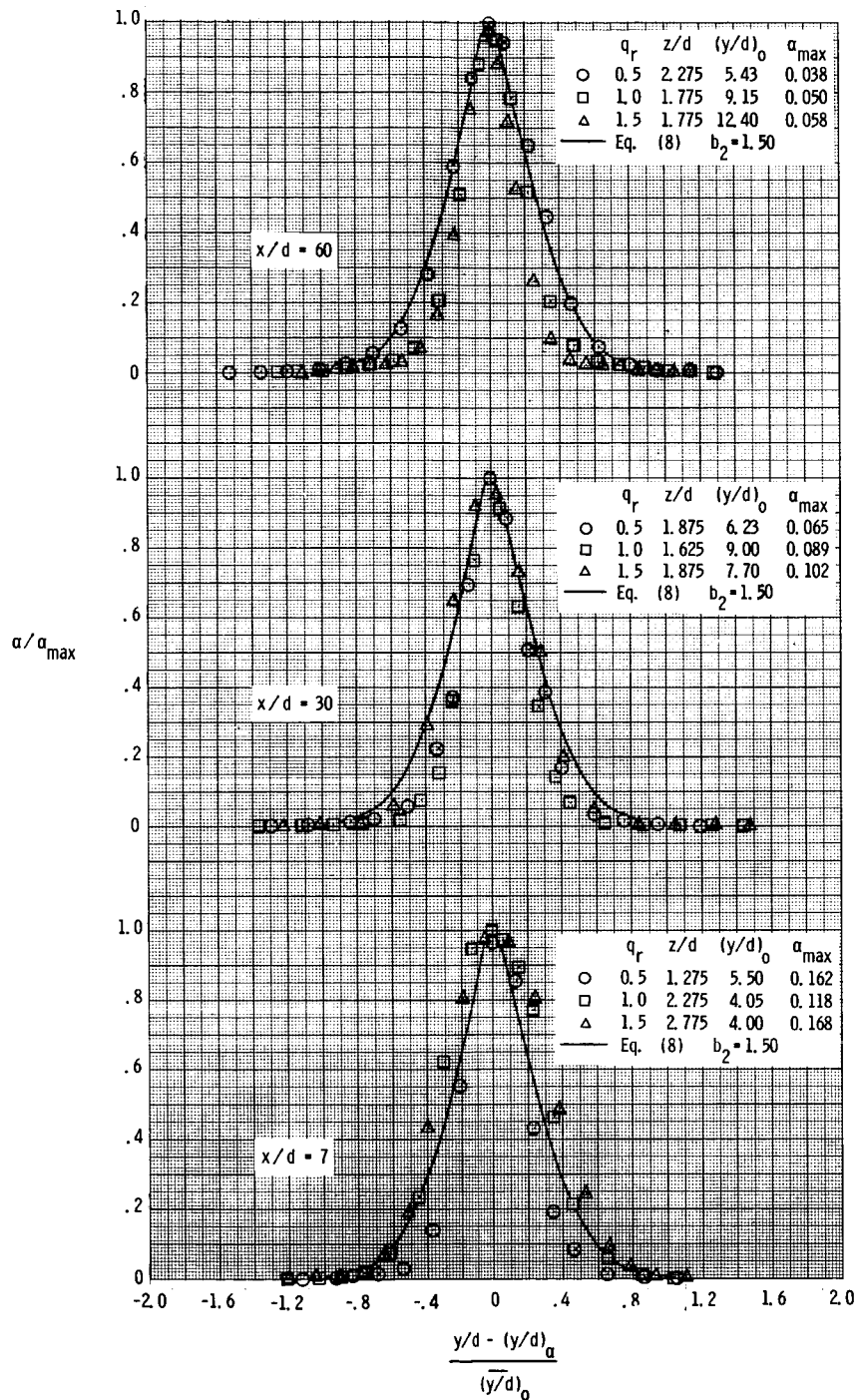
(b) $q_r = 1.0$.

Figure 13.- Nondimensional total-pressure profiles. Vertical survey.



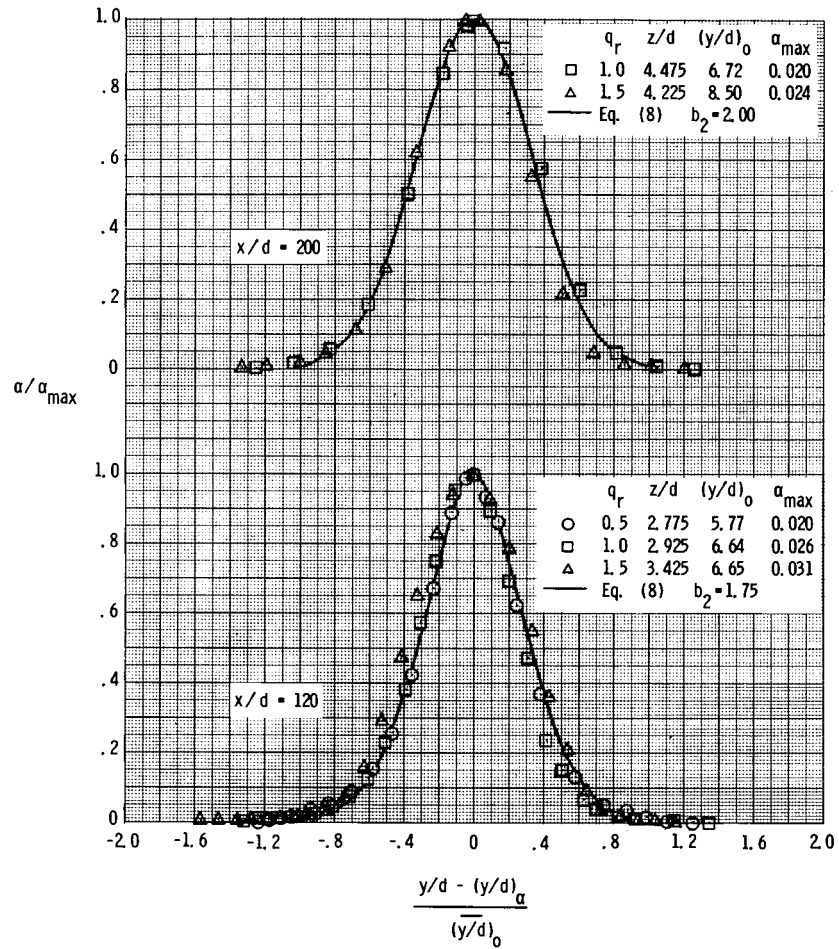
(c) $q_r = 1.5$.

Figure 13.- Concluded.



(a) $x/d = 7, 30, \text{ and } 60$.

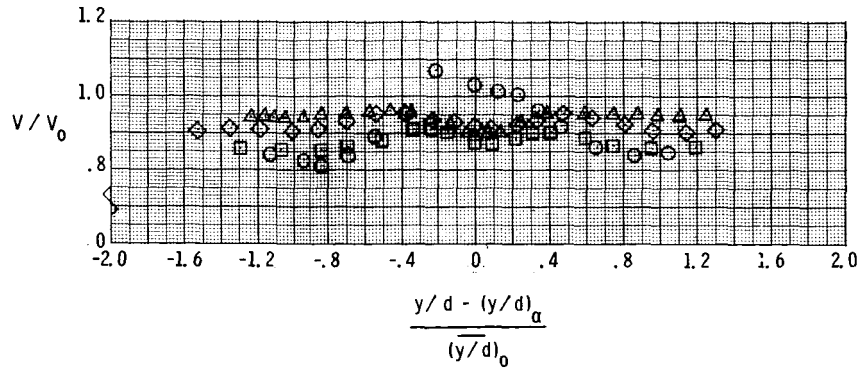
Figure 14.- Nondimensional concentration profiles. Horizontal survey through point of maximum concentration.



(b) $x/d = 120$ and 200 .

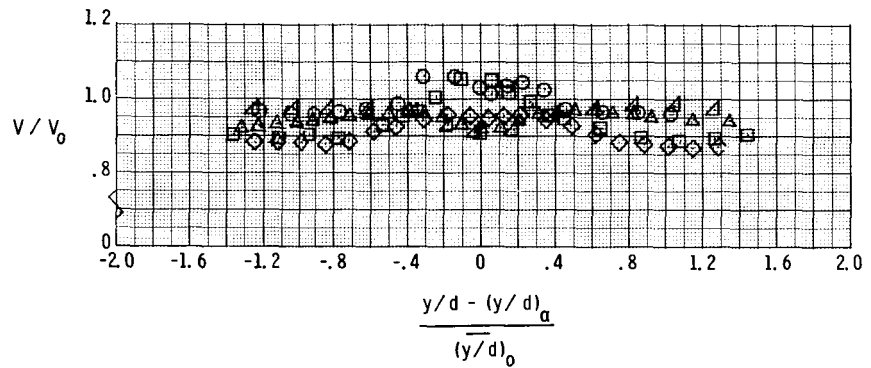
Figure 14.- Concluded.

x/d	z/d	(y/d) ₀	V ₀ , m/sec	
○	7	1.275	5.50	646.7
□	30	1.875	6.23	653.1
◇	60	2.275	5.43	668.1
△	120	2.775	5.77	674.5



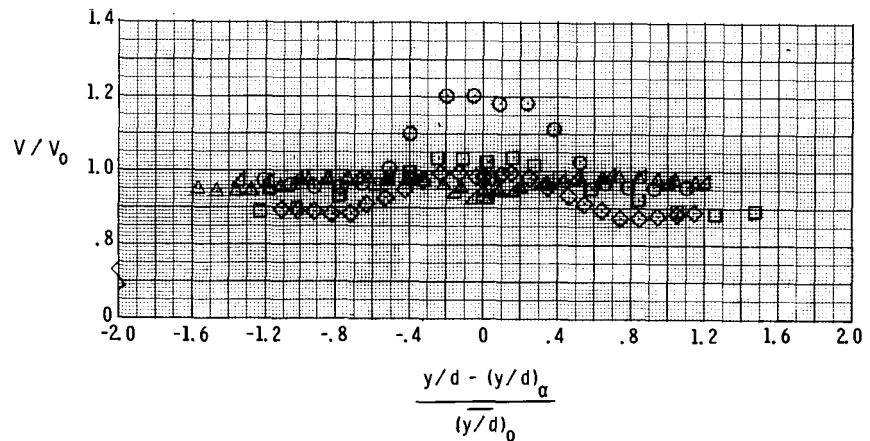
(a) $q_r = 0.5$.

x/d	z/d	(y/d) ₀	V ₀ , m/sec	
○	7	2.275	4.05	659.1
□	30	1.625	9.00	646.0
◇	60	1.775	9.15	668.7
△	120	2.925	6.64	671.1
△	200	4.475	6.72	654.6



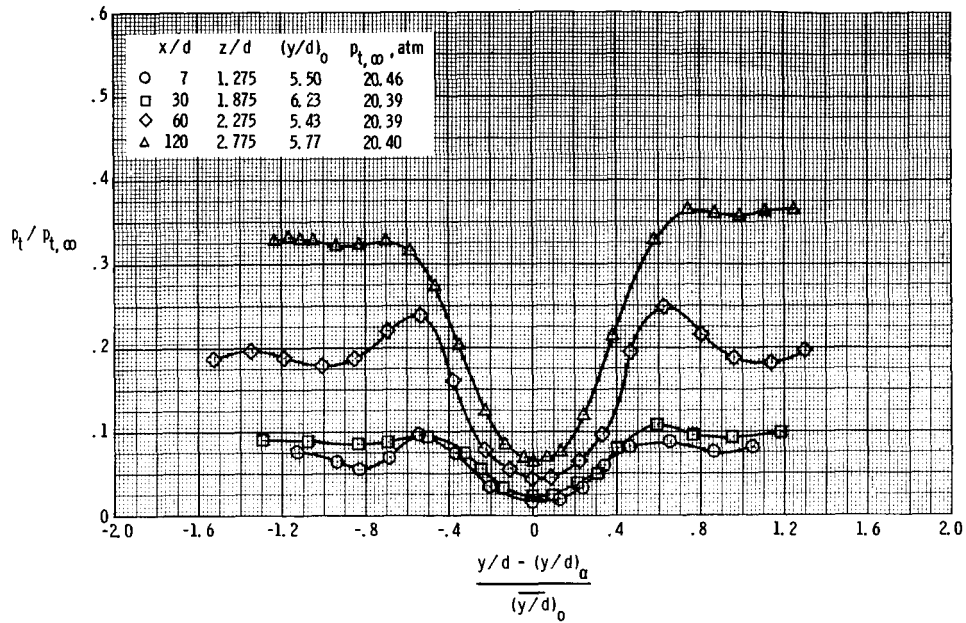
(b) $q_r = 1.0$.

x/d	z/d	(y/d) ₀	V ₀ , m/sec	
○	7	2.775	4.00	674.6
□	30	1.875	7.70	645.7
◇	60	1.775	12.40	661.2
△	120	3.425	6.65	675.6
△	200	4.225	8.50	658.8

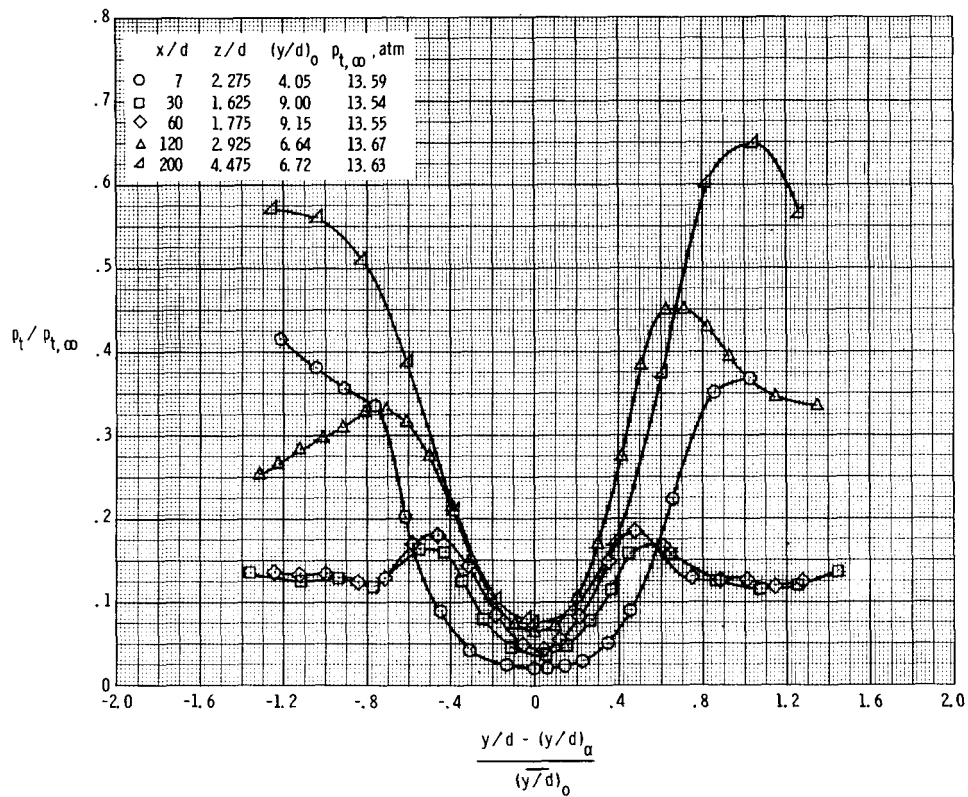


(c) $q_r = 1.5$.

Figure 15.- Nondimensional velocity profiles. Horizontal survey through point of maximum concentration.

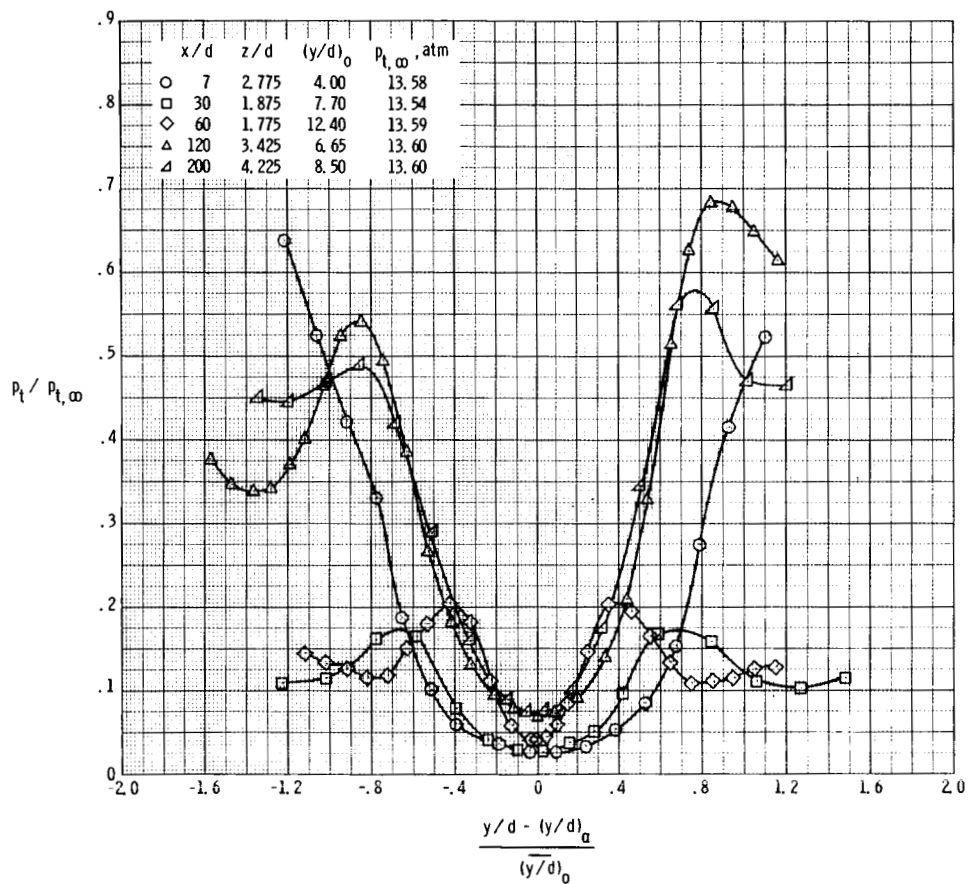


(a) $q_r = 0.5$.



(b) $q_r = 1.0$.

Figure 16.- Nondimensional total-pressure profiles. Horizontal survey through point of maximum concentration.



(c) $q_r = 1.5$.

Figure 16.- Concluded.

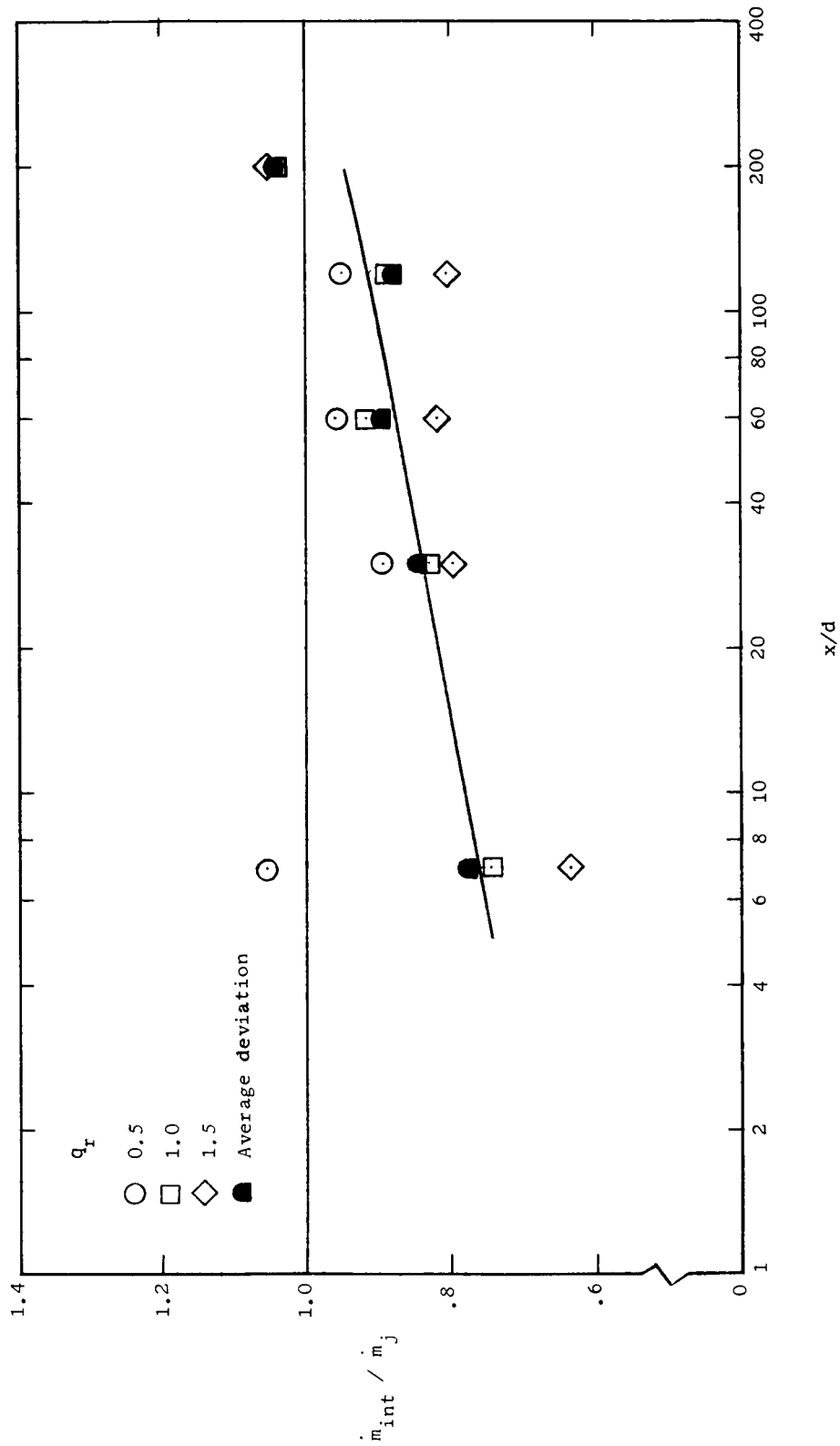
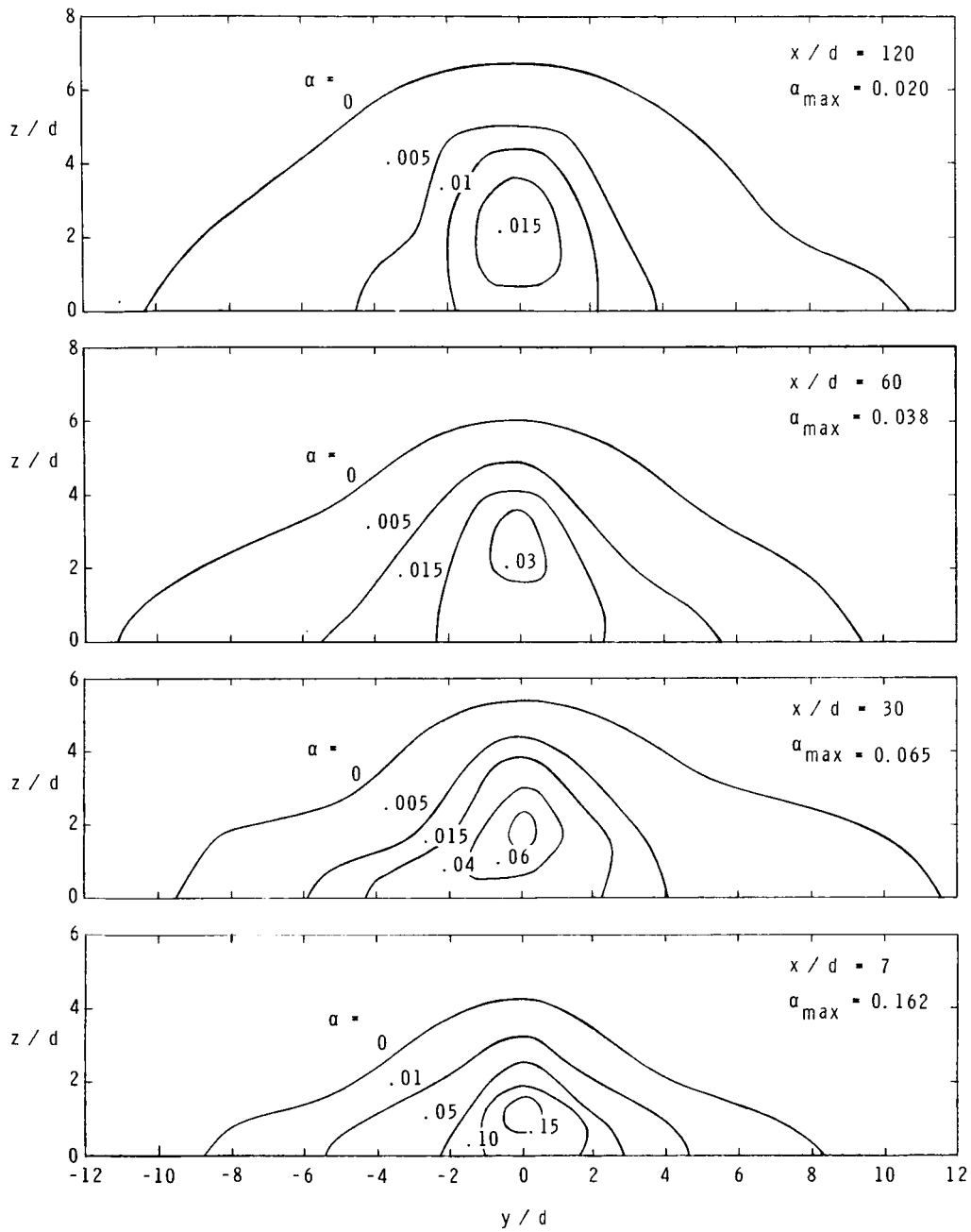


Figure 17.- Results of fuel mass flow contour integration.



(a) $q_r = 0.5$.

Figure 18.- Hydrogen mass fraction contours.

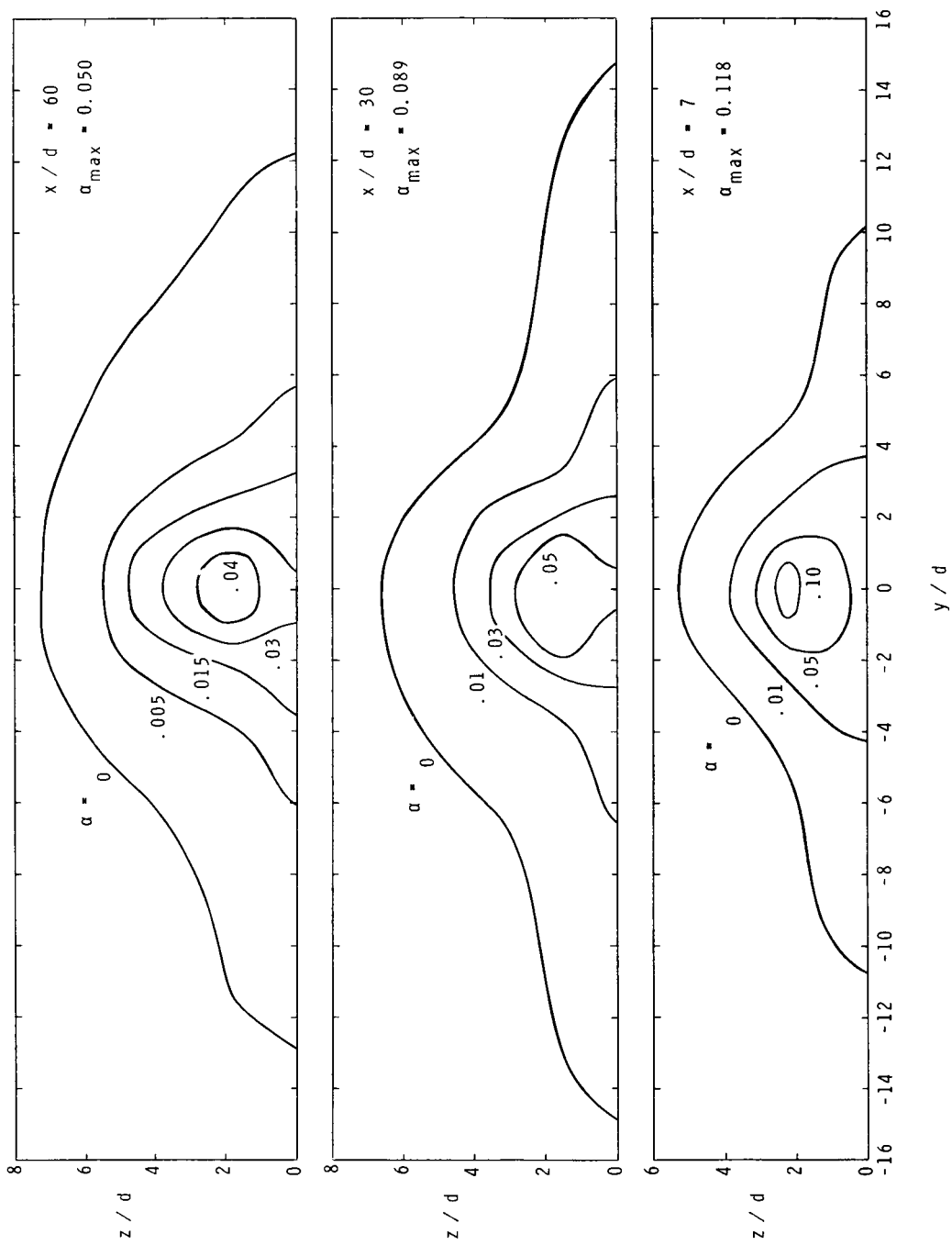
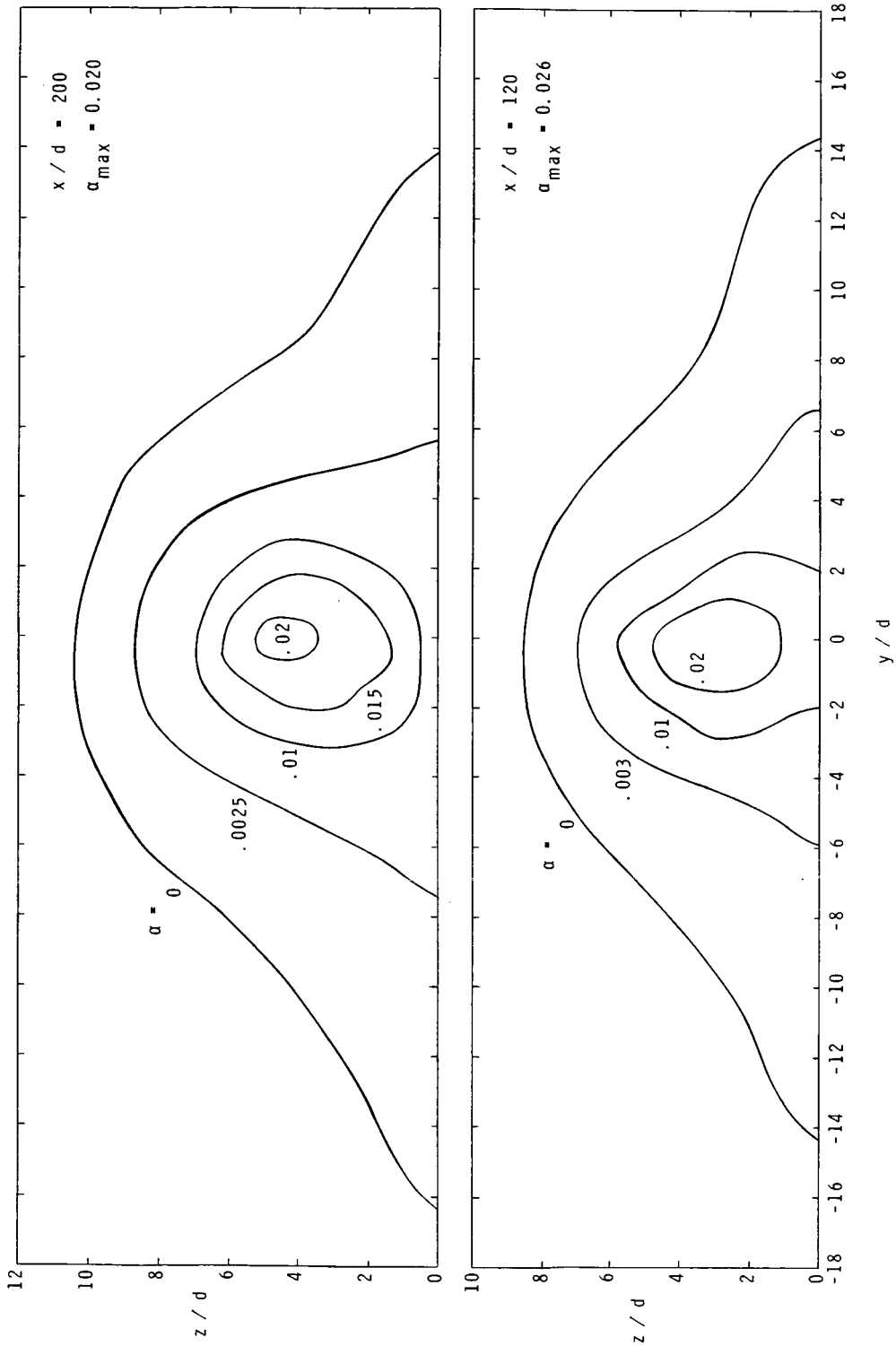
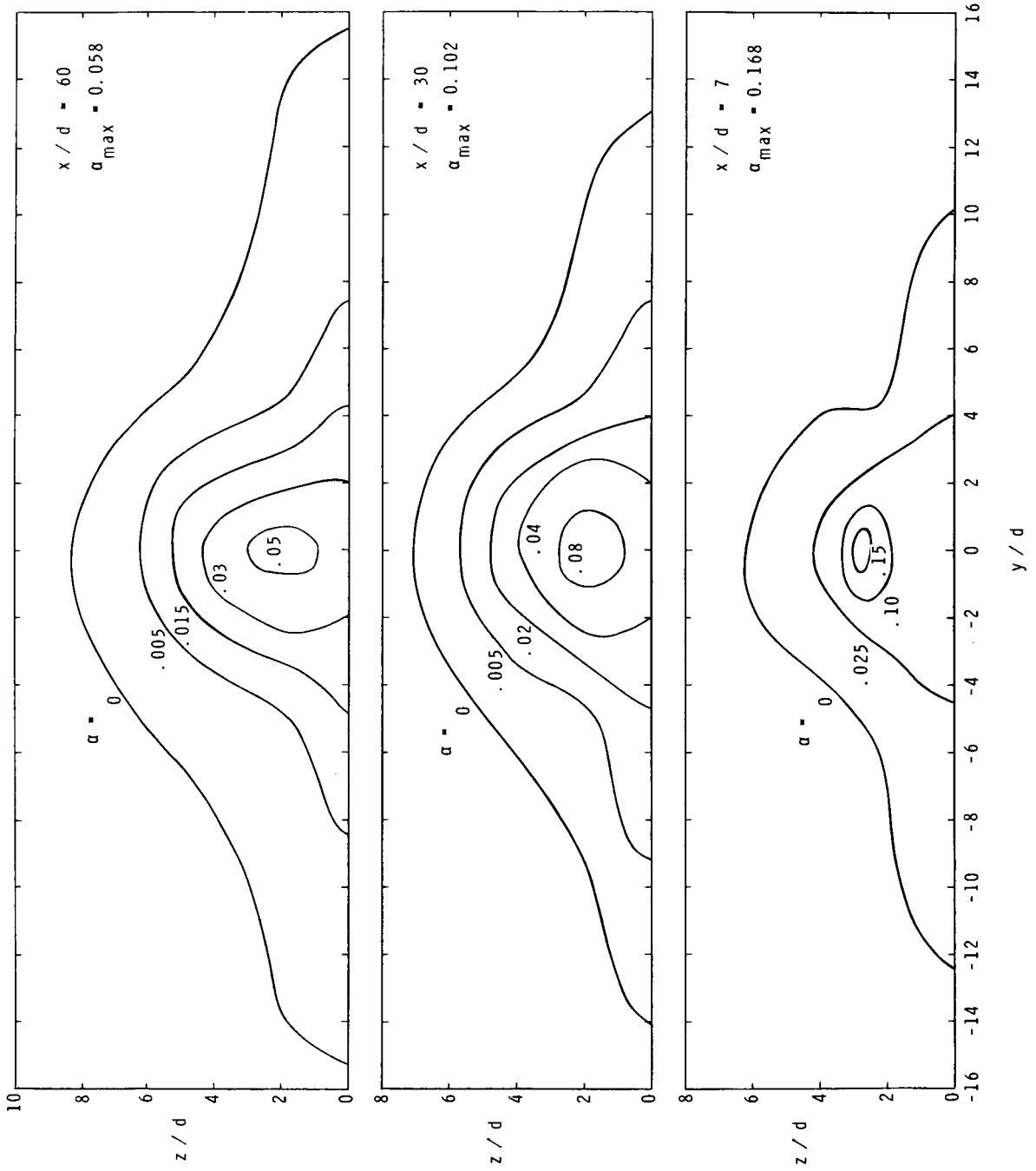
(b) $q_r = 1.0$.

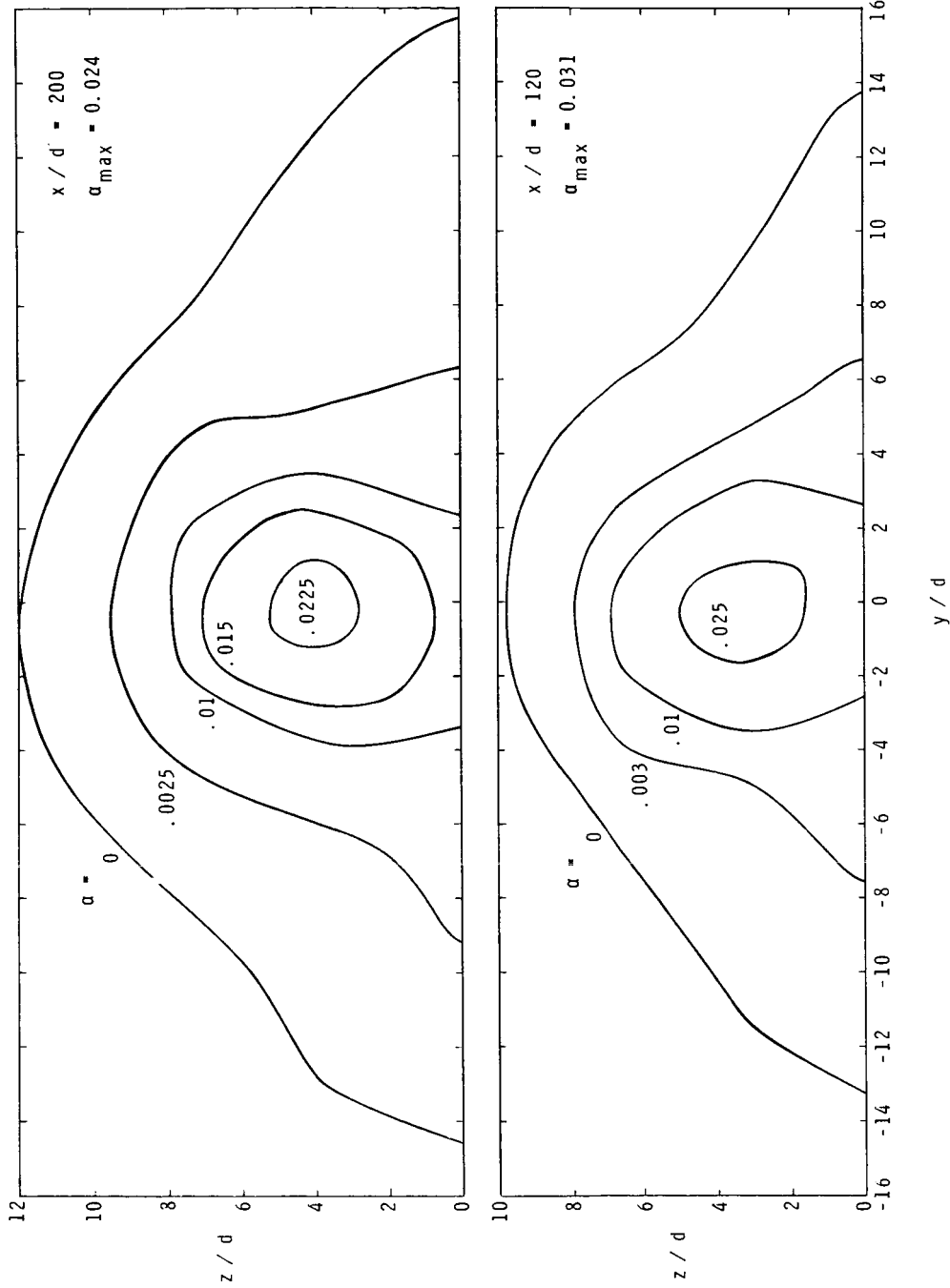
Figure 18.- Continued.



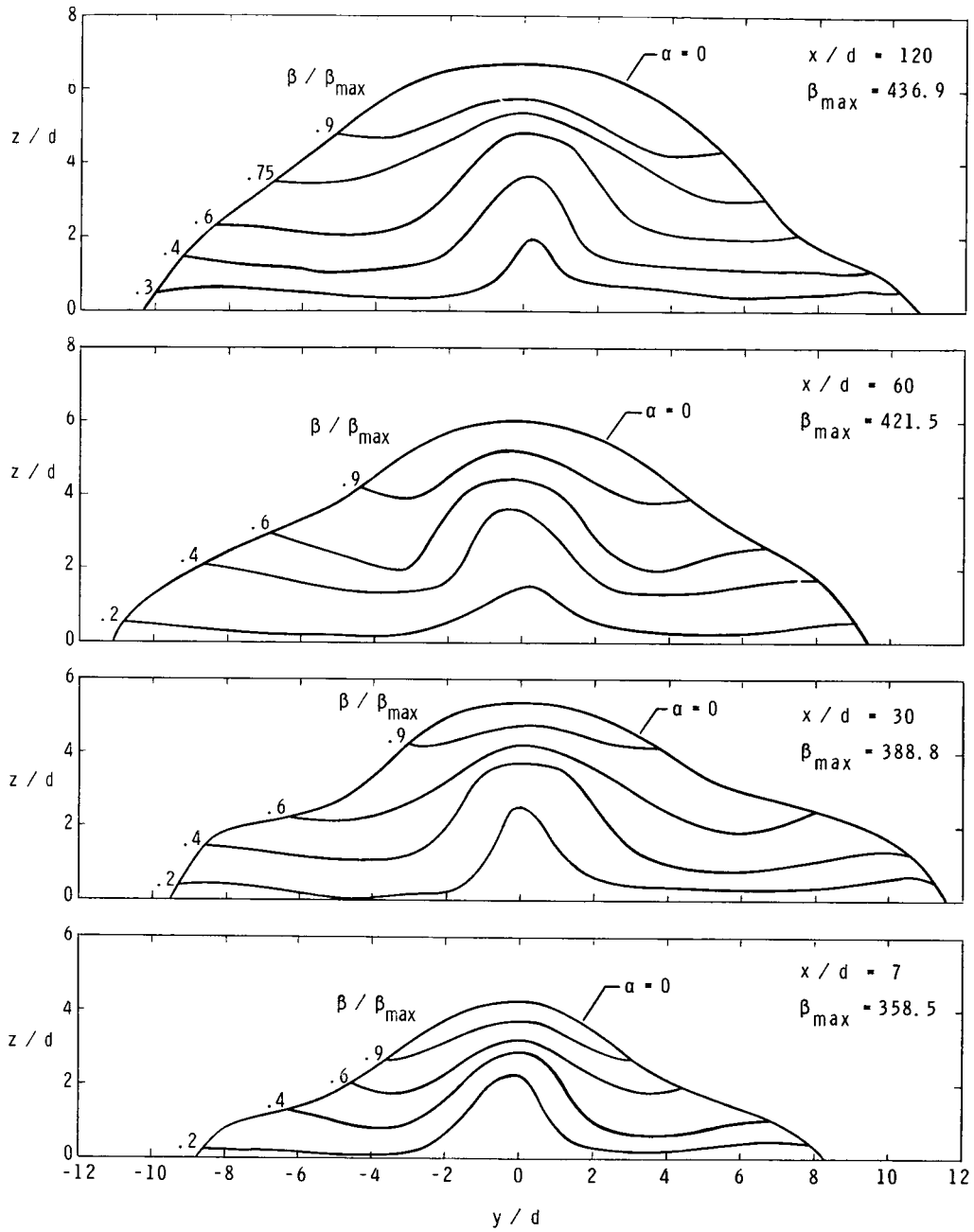
(b) $q_r = 1.0$. Concluded.
 Figure 18.- Continued.



(c) $q_r = 1.5$.
 Figure 18. - Continued.

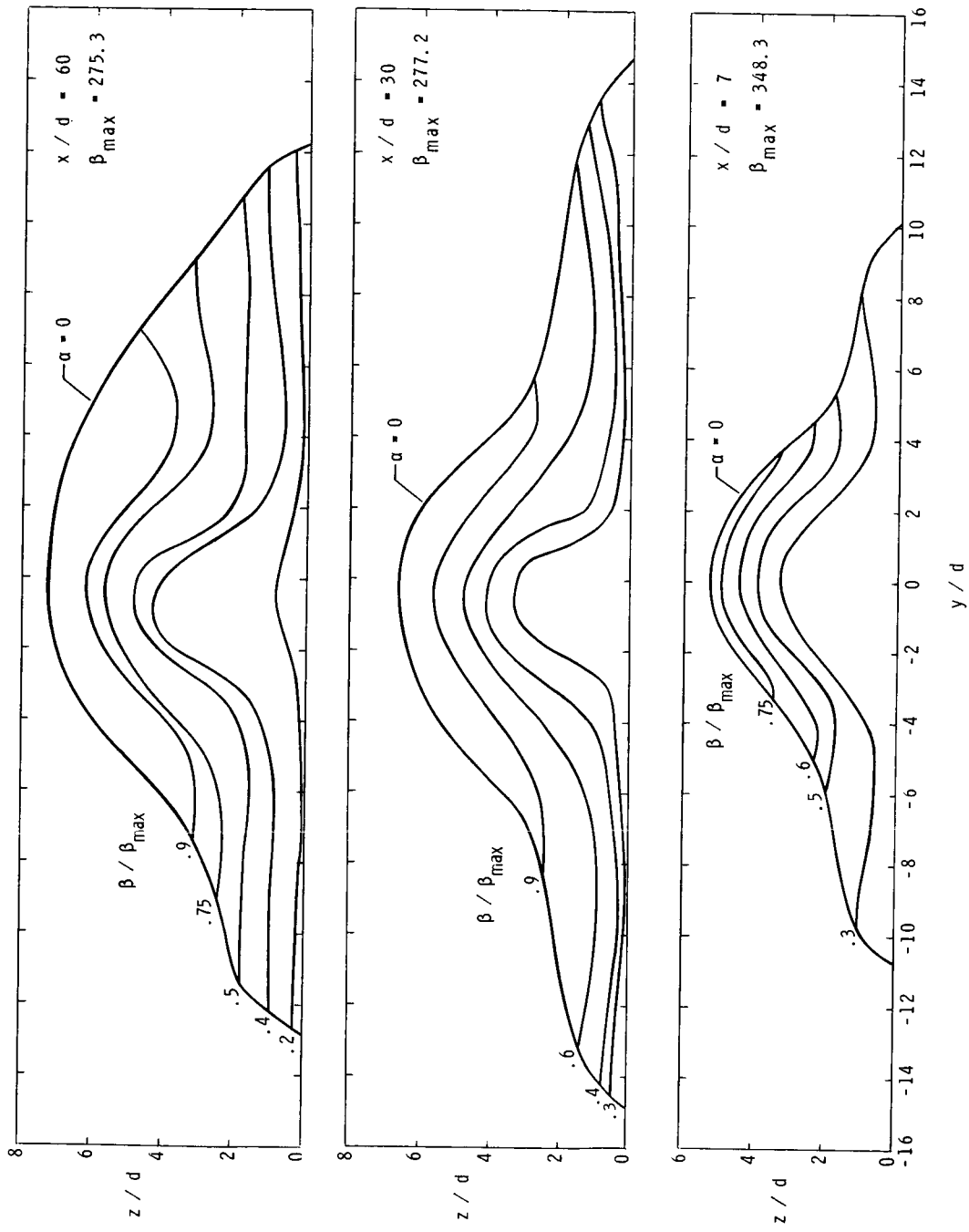


(c) $q_r = 1.5$. Concluded.
 Figure 18.- Concluded.

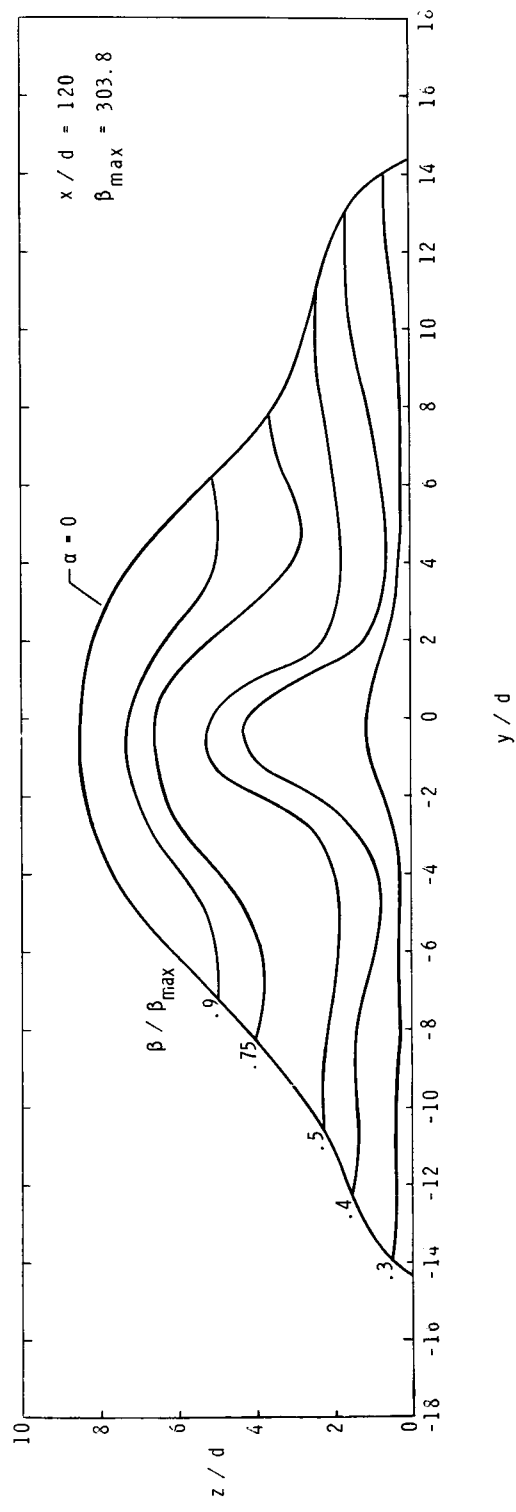
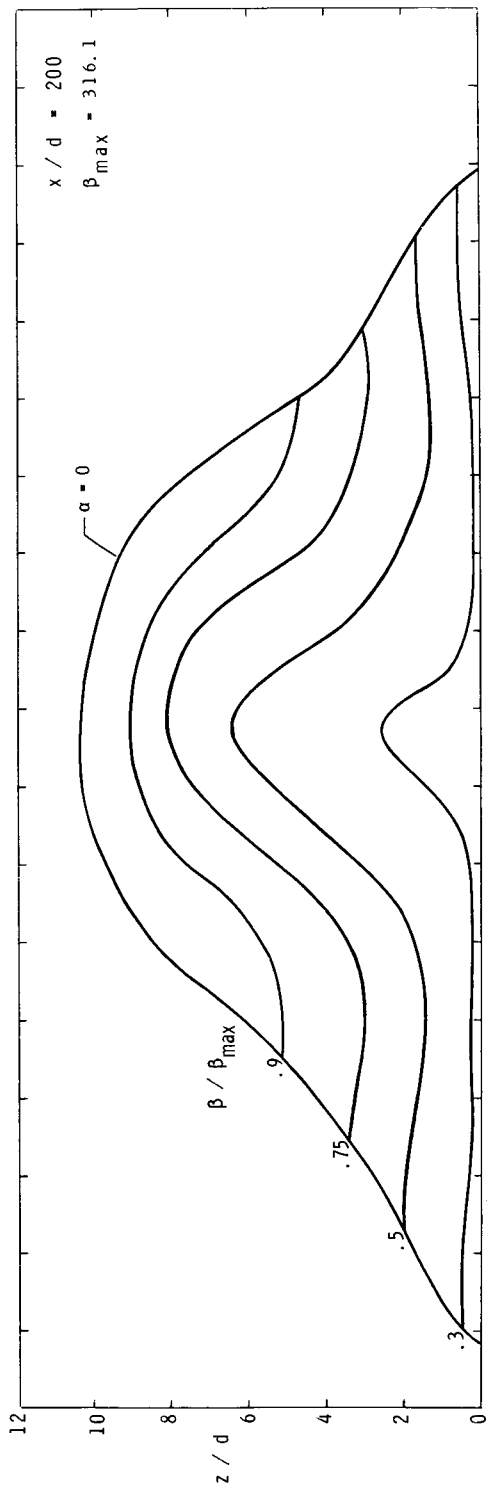


(a) $q_r = 0.5$.

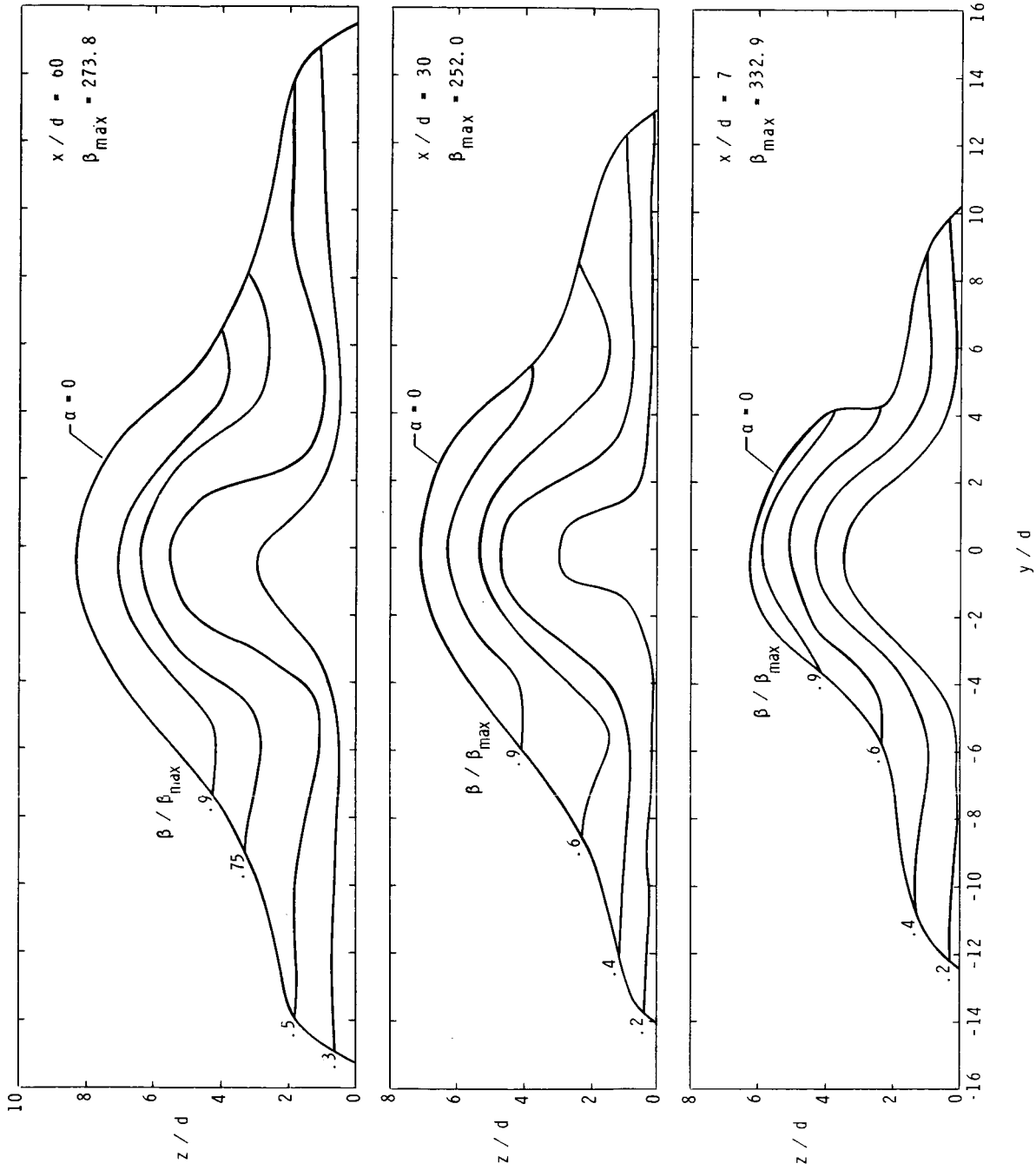
Figure 19.- Air mass flow contours.



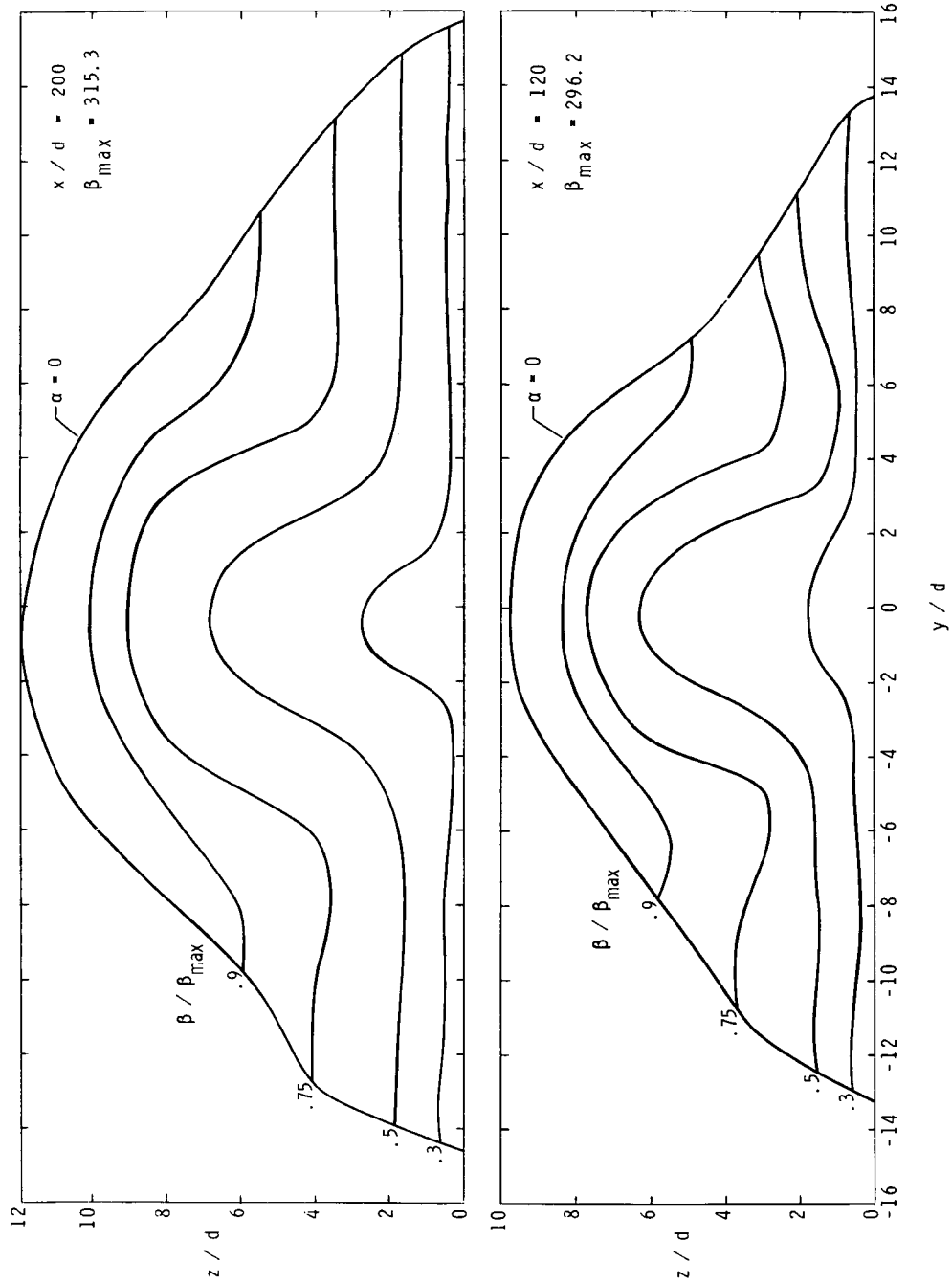
(b) $q_r = 1.0$.
 Figure 19.- Continued.



(b) $q_r = 1.0$. Concluded.
 Figure 19.- Continued.



(c) $q_r = 1.5$.
Figure 19. - Continued.



(c) $q_r = 1.5$. Concluded.

Figure 19.- Concluded.

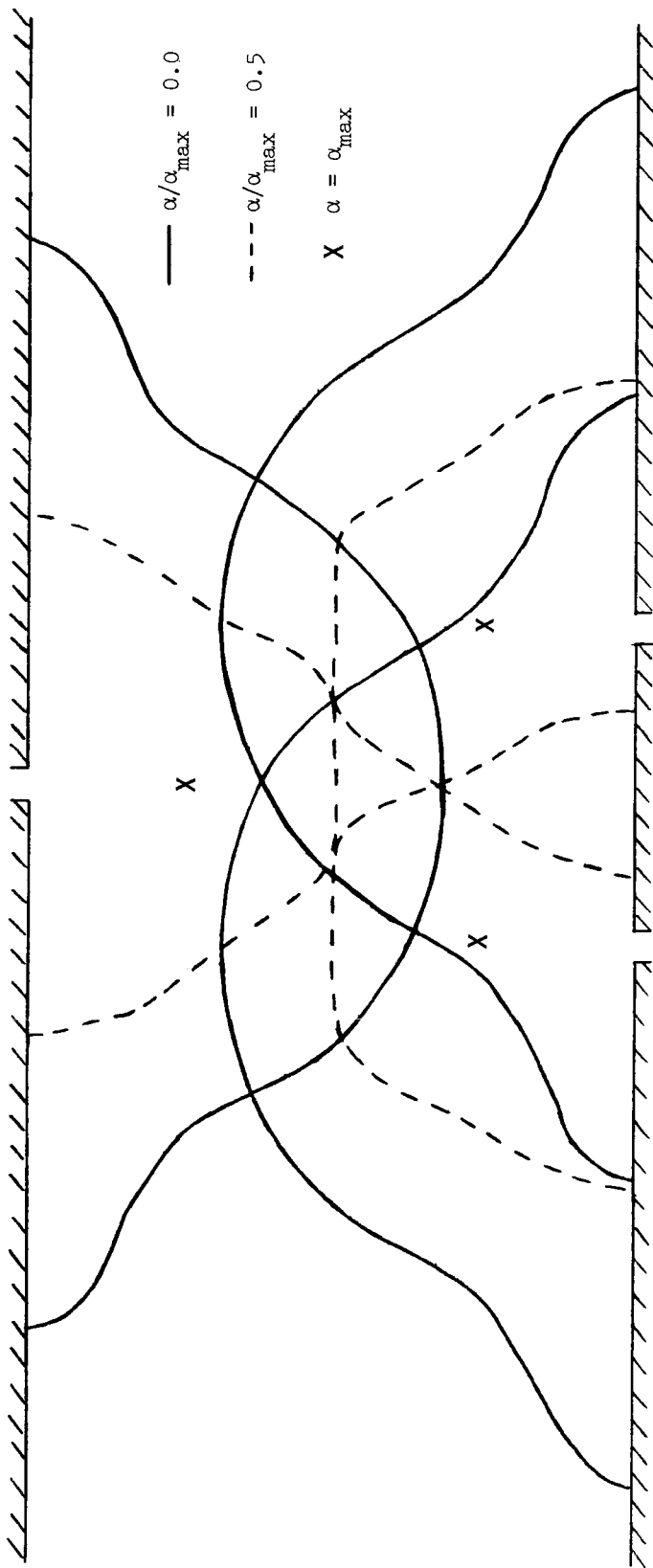


Figure 20.- Schematic of flow-field cross section for opposite staggered injection by superposition of single jet contours.

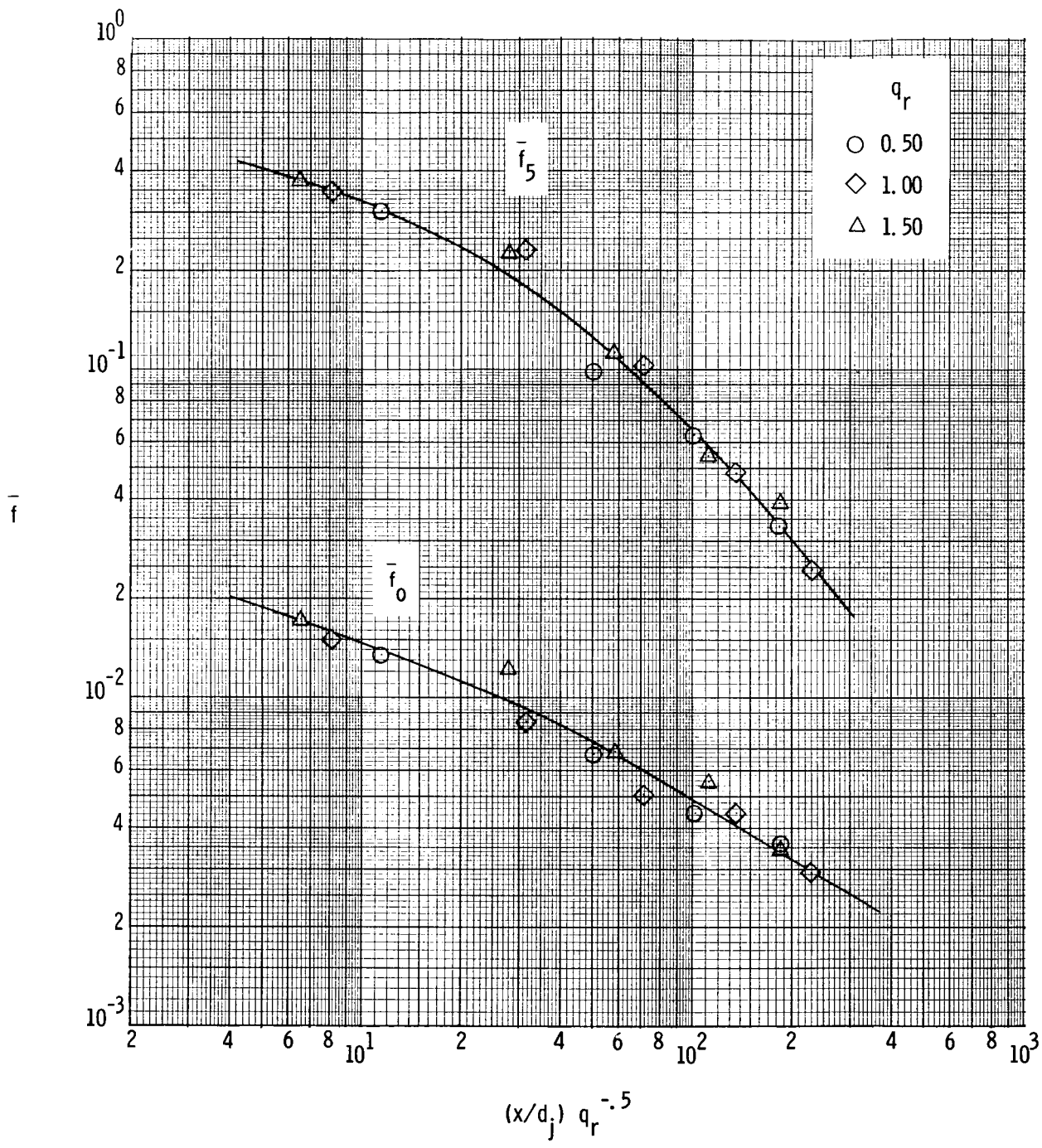


Figure 21.- Average fuel-air ratio decay.

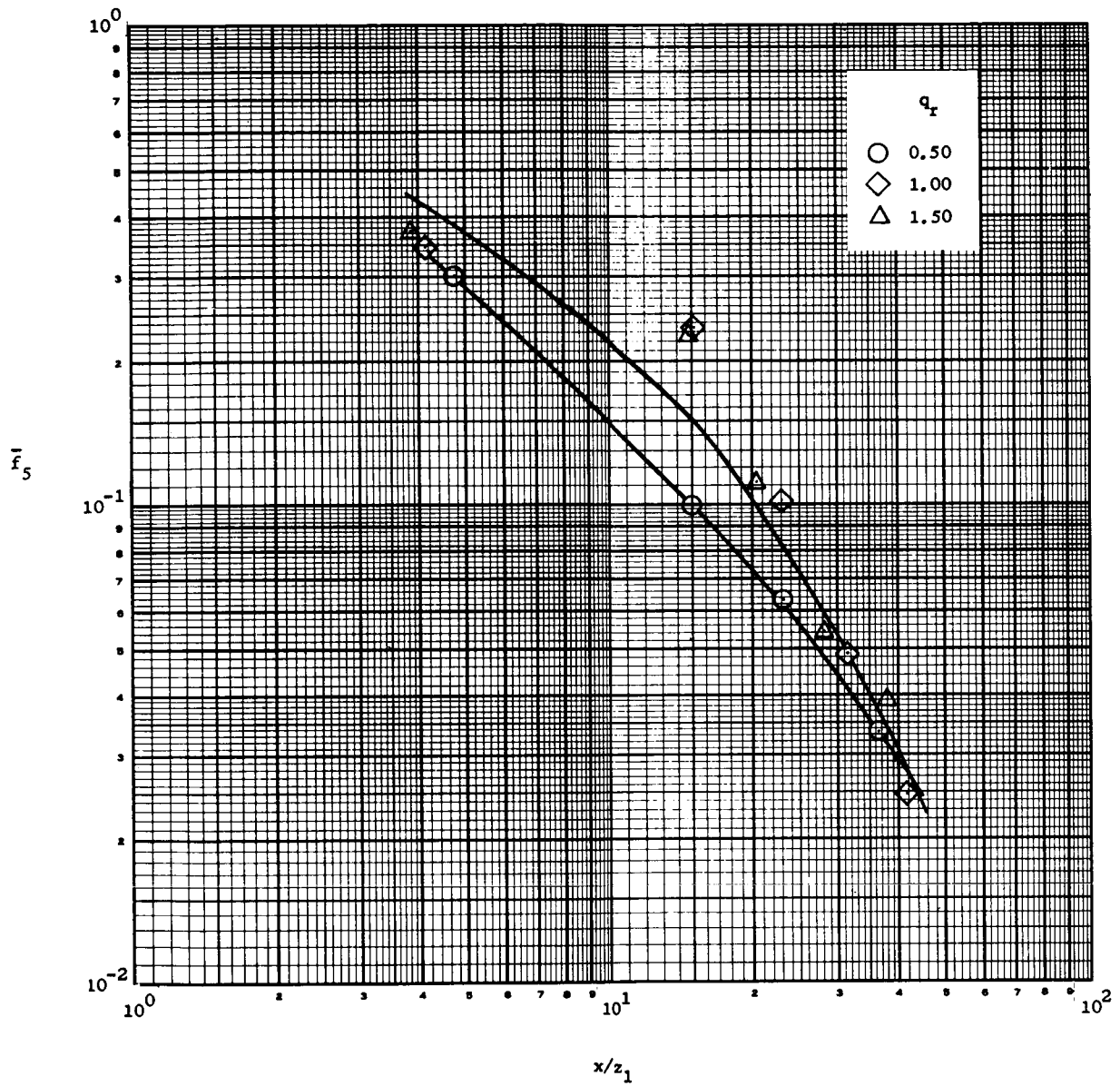


Figure 22. - Decay of average fuel-air ratio for simulated opposite wall injection.